Synthesis, SC-XRD structure, spectroscopy, intermolecular interactions, DFT/TD-DFT investigation, and (static, dynamic) NLO properties of (2E,5Z)-3-(4-fluorophenyl)-2-(4-fluorophen...

Article *in* Journal of Molecular Structure · November 2023

DOI: 10.1016/j.molstruc.2023.136967

Rachida Rahmani
Ahmed Zabana University, Relizane, Algeria.
27 PUBLICATIONS **298** CITATIONS

Guerroudj Ahlam Roufieda
Université Abdelhamid Ibn Badis Mostaganem
9 PUBLICATIONS **51** CITATIONS

Ayada Djafri
University of Oran
79 PUBLICATIONS **915** CITATIONS

Abdelkader Chouaih
Université Abdelhamid Ibn Badis Mostaganem
111 PUBLICATIONS **762** CITATIONS

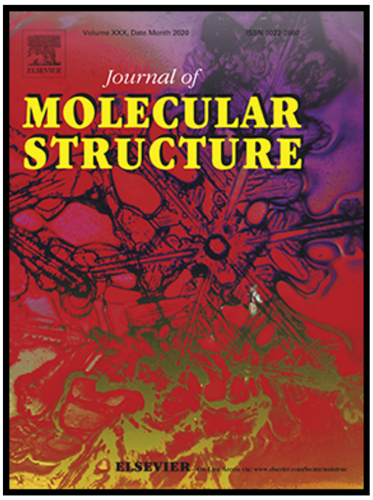

Synthesis, SC-XRD structure, spectroscopy, intermolecular interactions, DFT/TD-DFT investigation, and (static, dynamic) NLO properties of (2E,5Z)-3-(4-fluorophenyl)-2-(4-fluorophenylimino)-5-((E)-3-(2-nitrophenyl) allyliden) thiazolidin-4-one

Narimane Kheddam , Ahmed Djafri , Youcef Megrouss ,
Rachida Rahmani , Ahlam Roufieda Guerroudj ,
Soumia Belhachemi , Ayada Djafri , Abdelkader Chouaih

PII: S0022-2860(23)02057-4
DOI: https://doi.org/10.1016/j.molstruc.2023.136967
Reference: MOLSTR 136967

To appear in: *Journal of Molecular Structure*

Received date: 22 August 2023
Revised date: 22 October 2023
Accepted date: 29 October 2023

Please cite this article as: Narimane Kheddam , Ahmed Djafri , Youcef Megrouss , Rachida Rahmani , Ahlam Roufieda Guerroudj , Soumia Belhachemi , Ayada Djafri , Abdelkader Chouaih , Synthesis, SC-XRD structure, spectroscopy, intermolecular interactions, DFT/TD-DFT investigation, and (static, dynamic) NLO properties of (2E,5Z)-3-(4-fluorophenyl)-2-(4-fluorophenylimino)-5-((E)-3-(2-nitrophenyl) allyliden) thiazolidin-4-one, *Journal of Molecular Structure* (2023), doi: https://doi.org/10.1016/j.molstruc.2023.136967

Highlights

- New thiazolidinone derivative was synthesized and characterized by ^{1}H and ^{13}C NMR.
- Its molecular structure has been determined by X-ray crystallography and DFT.
- To display the intermolecular interactions, the Hirshfeld surface, and RDG were used.
- B3LYP and CAM- B3LYP functionals were used to study HOMO-LUMO, GRCD, and MEP.
- Thermodynamic properties were calculated.
- Static and dynamic nonlinear optical parameters were predicted using DFT approach.

Synthesis, SC-XRD structure, spectroscopy, intermolecular interactions, DFT/TD-DFT investigation, and (static, dynamic) NLO properties of (2E,5Z)-3-(4-fluorophenyl)-2-(4-fluorophenylimino)-5-((E)-3-(2-nitrophenyl) allyliden) thiazolidin-4-one

Narimane Kheddam[1,2], Ahmed Djafri[1,3], Youcef Megrouss[1,4], Rachida Rahmani[1,5], Ahlam Roufieda Guerroudj[1], Soumia Belhachemi[1,6], Ayada Djafri[7], Abdelkader Chouaih[1,*]

[1] Laboratory of Technology and Solid Properties (LTPS), Faculty of Sciences and Technology, Abdelhamid Ibn Badis University of Mostaganem, 27000 Mostaganem, Algeria

[2] Faculty of Medicine, Abdelhamid Ibn Badis University of Mostaganem, 27000 Mostaganem, Algeria

[3] Centre de Recherche Scientifique et Technique en Analyses Physico-chimiques (CRAPC), BP 384-Bou-Ismail-RP, 42004 Tipaza, Algeria

[4] Chemistry Department, Faculty of Exact Sciences and Informatic, Hassiba Benbouali University, Chlef 02000, Algeria

[5] Department of Process Engineering, Faculty of Sciences and Technology, Ahmed Zabana - University of Relizane, Relizane, Algeria

[6] Chemistry Department, Faculty of Exact Sciences and Informatic, Abdelhamid Ibn Badis University of Mostaganem, 27000 Mostaganem, Algeria

[7] Laboratoire de Synthèse Organique Appliquée, Faculté des Sciences Exactes et Appliquées, Département de Chimie, Université Oran-1, 31000 Oran, Algeria

* Corresponding author: achouaih@gmail.com, abdelkader.chouaih@univ-mosta.dz

Abstract

This paper describes the synthesis of a novel fluorine-substituted thiazolidin-4-one compound, (2E,5Z) -3-(4-fluorophenyl) -2-(4-fluorophenylimino) -5-((E)-3-(2-nitrophenyl) allyliden) thiazolidin-4-one, abbreviated as F2NTh. Its structure was subsequently characterized by Fourier transform infrared (FTIR), ^{1}H and ^{13}C nuclear magnetic resonance (NMR), UV-Visible, and single crystal X-ray diffraction (SC-XRD). For a better comprehension of the electronic structure of F2NTh, experimental data collected from the X-ray diffraction pattern were then compared to theoretical results computed by the density functional theory (DFT) using both B3LYP and CAM-B3LYP functionals with a 6-311G (d, p) basis set. Theoretical results exhibited a good correlation with those established through the experimental analysis. To identify intra- and intermolecular interactions, Hirshfeld surface (HS) and reduced density gradient (RDG) analyses were performed. The results, including 2D fingerprint plots, indicated that H...H interactions played a major role, accounting for 23.6% of the overall intermolecular contacts. To investigate the charge transfer and ascertain the electronic properties of F2NTh, frontier molecular orbitals and global and local chemical reactivity descriptors were studied. By simulating the molecular electrostatic potential (MEP) and using MPA, NPA, ESP, and MC5 atomic charges, reactive sites within the molecule responsible for electrophilic and nucleophilic attacks were identified. Some thermodynamic parameters and functions (enthalpy, heat capacity, and entropy) obtained from spectroscopic data were also examined in the temperature range of 100–1000 K. Finally, to test the title molecule in the non-linear optical (NLO) domain, the corresponding properties were predicted using B3LYP and CAM-B3LYP functionals. The predicted static NLO parameters (μ = 4.93 D, α = 56.23×10^{-24} esu, β = 28×10^{-30} esu, and γ = 244.98 ×10^{-36} esu) revealed highly promising outcomes, exhibiting the molecule's utility in NLO applications. This activity was confirmed by the dynamic NLO parameters showing a high third-order response.

Keywords

Thiazolidin-4-ones, atomic charges, MEP, HS, RDG, dynamic NLO, Fukui, reactivity.

1. Introduction

Organic heterocyclic molecules play a crucial role in various biological and catalytic activities **[1-3]**. These molecules are designed and optimized to exhibit high catalytic activity, selectivity, and stability, making them useful in various fields such as medicine, agriculture, and materials science **[4-8]**. Understanding the factors that influence their catalytic performance is essential for further advancements in the field of organic synthesis and catalysis **[9-13]**. Additionally, organic molecules also serve as homogenous and/or heterogeneous catalysts in numerous chemical reactions, accelerating the rate of these reactions **[14-18]**. Recently, the interest in non-linear optical materials (NLO) in the scientific world has been steadily increasing due to their impact in a wide variety of fields such as optical data transmission, optical data storage, optical signal processing, optical communication, second harmonic generation, lasers, refractive index modulation, optical switching, and optical limiting **[19]**. NLO includes a range of materials, such as small organic molecules, polymers, and inorganic crystals. Among the class of substances that have a meaningful NLO potential are thiazolidinone and its derivatives. These molecules exhibit a vast array of biological activities in addition to their non-linear optical properties **[20, 21]**. These include anti-cancer agents **[22]**, analgesics and anti-inflammatory agents **[23]**, antimicrobials and antiparasitics **[24, 25]**, antivirals **[26]**, anticonvulsants **[27]** antidiabetics **[28]**, and anti-HIV agents **[29]**. The electronic structure of these molecules gives them significant biological potential **[30]**. Indeed, many studies have shown that the presence of heteroatoms within these molecules directly influences the structure, electronic, and optic properties, including the charge transfer phenomena that take place throughout the conjugated system contained in the thiazolidinones **[31, 32]**. These give rise to inter- and intramolecular interactions that subsequently allow the molecule to be an effective agent with a higher NLO effect **[20]**. The heteroatom in the thiazolidinone molecule is the privileged site of electrophilic attack in a state of sp^3 hybridization and the privileged site of nucleophilic attack in a state of sp^2 hybridization **[33]**. The high electronic concentration around the heteroatom allows for more intermolecular bonds formation. These intermolecular bonds contribute to the overall stability and strength of the molecule. Additionally, the high electronic concentration also enhances the reactivity of the heteroatom, making the molecule a potential candidate for applications in electronic and optical devices.

In this context, with the aim of investigating the impact of the most electronegative chemical element, fluorine, as well as the inductive and mesomeric electronic effects and highly attractive character of the nitro group, the synthesis of the novel derivative (2E,5Z)-3-(4-

fluorophenyl)-2-(4-fluorophenylimino)-5-((E)-3-(2-nitrophenyl)allyliden) was performed. The thiazolidin-4-one derivative was then characterized using experimental techniques such as SC-XRD, FT-IR, ^{1}H and ^{13}C NMR, and UV-visible spectroscopy. Additionally, we have achieved in this work quantum chemical calculations at the ground state of the title molecule. The theoretical study was performed by the DFT method using the three-parameter hybrid Becke-Yang-part (B3LYP) and the Coulomb attenuated method-B3LYP (CAM-B3LYP) functionals along with a 6-311G(d, p) basis set. It is well known that the B3LYP functional **[34, 35]** is the most popular functional used in the quantum chemical literature today that usually provides plausible results **[36–38]**. This functional was found in several works **[39, 40]** that, in some cases, failed to reproduce computed spectra similar to the experimental ones within the context of studying other interesting parameters. Within this framework, the CAM-B3LYP functional **[41]**, which is a separate version of B3LYP, has enabled the study of certain parameters to be improved, particularly the UV-visible spectra, NLO, and thermodynamic predictions **[42, 43]**. The main improvement of the CAM-B3LYP functional is the incorporation of a post-Hartree-Fock correction of coupled cluster theory. This correction takes into account electron correlation effects that are not fully accounted for by standard DFT functionals such as B3LYP. It improves the accuracy of CAM-B3LYP in describing difficult electron correlation phenomena, such as dispersion forces and weak interactions. CAM-B3LYP generally includes improved dispersion correction terms compared to the standard B3LYP functional. Dispersion strengths are additionally crucial for precise modeling of non-covalent interactions like van der Waals interactions. Accurate modeling of van der Waals interactions requires understanding the dispersion strengths between the interacting species. For optimal results, we used both functionals in theoretical calculations. Following the structural analysis, several parameters closely related to the three-dimensional structure of F2NTh were determined. Hirshfeld surface analysis and 2D fingerprint plots were performed in order to understand and visualize the relative contributions of different non-bonded contacts in the crystal structure. The reduced density gradient (RDG) analysis was used to explore the nature of repulsive and attractive van der Waals interactions. Furthermore, to support experimental results and to better understand the electronic, structural, and optical properties of the investigated molecule, HOMO and LUMO energies were determined using density of states analysis to confirm the charge transfer occurred in the title molecule. Thermodynamic properties and global and local chemical reactivity descriptors were also calculated. Atomic charges were computed with four different models, including Mulliken (MPA), natural population analysis (NPA), Hirshfeld (MC5), and Merz-Kollman (ESP) charges, where the advantages and disadvantages of each model were exposed. This comparative study of atomic charges allowed us to better interpret the nucleophilic and electrophilic behavior of the title compound and to determine the most active molecular sites to predict the interactions and reactions that the F2NTh molecule might produce. By the end of this study, we confirmed the potential of our molecule in the NLO field by calculating the dipole moment (μ), the average mean polarizability (α), the first-order hyperpolarizability (β), and the second-order hyperpolarizability (γ) by means of B3LYP and CAM-B3LYP/6-311 G (d, p) levels of theory.

2. Experimental and computational approaches

2.1. *Synthesis of (2E,5Z)-3-(4-fluorophenyl)-2-(4-fluorophenylimino)-5-((E)-3-(2-nitrophenyl)allyliden)thiazolidin-4-one (F2NTh)*

The title compound was synthesized using the chemical pathways depicted in **Scheme 1**. 1, 3-bis-(4-fluorophenyl) thiourea (2) was synthesized by reacting 4-fluorobenzenamine (0.02 mol) (1) with carbon disulfide (0.01 mol) in dry ethanol (10 ml) and refluxing the mixture for 6 hours. The resulting compound **(2)** and ethyl bromoacetate were refluxed for 2 hours in 40 ml of absolute ethanol to give compound 3-N-(4-fluorophenyl)-2-N’-(4-fluorophenylimino)-thiazolidin-4-one **(3)**. To a solution of **(3)** (0.01 mol) in (10 ml) of acetic acid and three equivalents of anhydrous sodium acetate CH_3COONa was added 2-nitrophenylcinamaldehyde (0.01 mol). The solution was refluxed for 4 hours. The reactions were monitored by thin-layer chromatography (TLC) using $CH_2Cl_2/CH_3CO_2C_2H_5$ (9/1) as solvent. The solid obtained was filtered and washed with acetone to form (2E, 5Z)-3-(4-fluorophenyl)-2-(4-fluorophenylimino)-5-((E)-3-(2-nitro phenyl) allylidene) thiazolidin-4-one **(4)** with 85% yield.

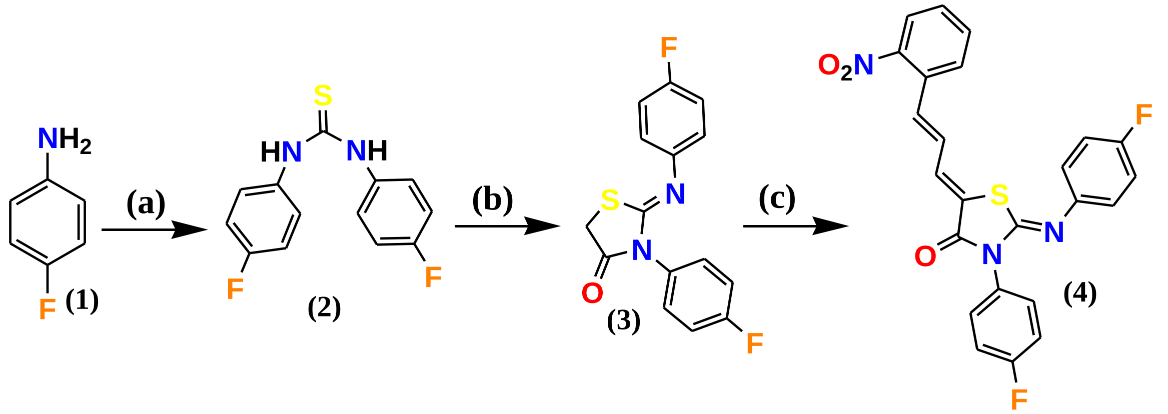

Reagents and conditions: (a): CS_2 , EtOH, Reflux(6h, 75°C); **(b):** $BrCH_2COOEt$, EtOH, Reflux(2h, 75°C); **(c):** $NO_2C_6H_4C_2H_2CHO$, CH_3COOH, CH_3COONa, Reflux(4h, 92°C)

Scheme 1. Synthesis pathway for F2NTh

2.2. *Spectroscopic data*

Yellow solid, mp = 190°C, IR **(KBr, cm^{-1})**: 2840 (C–H), 1720 (C=O), 1681 (C=N), 1571 (C=C), 1092 (C–N), 1214 (C–F), 505 (C–S). **^{1}H NMR, ($CDCl_3$, 300 MHz, δ (ppm), *J* (Hz)):** 6.64 (dd, 1H, *J* = 23.5 Hz, C–H), 7.28 (dd, 1H, C–H), 7.40 (dd, 1H, C–H), 7.03-8.13 (m, 11H, Ar–H); 9.80 (d, *J* = 7.6 Hz, 1H, Ar–H). ^{13}C **NMR, ($CDCl_3$, 300 MHz, δ (ppm)):** 122.25, 122.35, 122.44, 122.56, 127.49, 129.95, 130.02, 130.44, 131.16, 131.27, 132.64, 133.32, 133.85, 135.47, 136.46, 143.86, 143.89, 147.34, 155.55, 158.44, 161.66**,** 169.71, 170.58 (C=O), 171.32.

2.3. *Crystallographic insights*

The X-ray data of F2NTh was acquired by Nonius Kappa CCD using graphite monochromatic MoKα radiation (0.71073 Å), between about $1.53 \leq \theta \leq 25.67$, at ambient temperature (293 K). Direct methods implemented in the ShelxS **[44]** program were used to solve the structure. The ShelxL program **[45]** was used for the refinement, using the full matrix least squares method on F^2 with anisotropic thermal motion parameters for all atoms except hydrogen ones. The last full-matrix least-squares refinement gave R = 0.05, wR = 0.135, and S = 1.13 with all reflections and $I \geq 2\sigma$ (I). The molecular 3D structure and packing were produced using the ORTEP-3 **[46]** and Mercury **[47]** programs. Possible hydrogen bonds were evaluated using the PARST program **[48]**. The Hirshfeld surface (HS) and its related 2D fingerprint plots were made using Crystal Explorer 17.5 **[49]**. **Table 1** includes crystal structure data, measurement details, and refinement parameters for F2NTh.

Table 1

Experimental conditions and X-ray analysis details for F2NTh.

Chemical formula	$C_{24}H_{15}F_2N_3O_3S$
CCDC reference no	2287992
Molecular weight (g.mol^{-1})	463
Temperature (K)	293
Crystal dimensions (mm)	0.58 × 0.21 × 0.2
Radiation wavelength, MoKα (Å)	0.71073
Crystal System	Monoclinic
Space group, Z	$P2_1/c$, 4
a (Å)	13.780 (2)
b (Å)	7.872 (11)
c (Å)	20.422 (3)
β (°)	104.974 (4)
V (Å^3)	2140.3 (5)
Density g.cm^{-3}	1.448
μ (mm^{-1})	0.21
F (000)	956
θ range for data collection	[1.53 -25.67]
Limits of (h, k, l)	$-15 \leq h \leq 16$, $-9 \leq k \leq 9$, $-24 \leq l \leq 24$
No. of measured, independent and observed [$I \geq 2\sigma(I)$] reflections	24125, 4050, 3039
R_{int}	0.039
R [F2 > 2s(F2)], wR(F^2), S	0.0504, 0.1679, 1.130
Refinement parameters	258
$\Delta\rho_{min}$, $\Delta\rho_{max}$	-0.379, 0.557

2.4. *Spectral measurements and computational details*

The electronic absorption spectrum was registered on a Shimadzu UV-2600 Pc-spectrophotometer with a quartz cell of 1 cm using chloroform as solvent. The IR spectrum was obtained on a KBr tablet on a JASCO FT/IR 4210 Fourier Transform Infrared Spectrometer. ^{1}H and ^{13}C NMR were collected on a BRUKER AC DPX-200 spectrometer (300 MHz) using chloroform as a solvent and tetramethylsilane (TMS) as a standard inert reference.

All DFT calculations on F2NTh were performed using the Gaussian 09 software **[50]** and Gauss-View molecular visualization software **[51]**. Using the X-ray data, the initial structure was obtained, which was subsequently optimized by the DFT method with both B3LYP and CAM-B3LYP functionals using the 6-311G (d, p) basis set. The corresponding calculated vibrational frequencies were assigned by using the potential energy distribution (PED) with the VEDA 4 program **[52]**. The ^{1}H and ^{13}C NMR chemical shifts were determined using the standard gauge independent atomic orbital (GIAO) method **[53]**, referring to the TMS. Through the Multiwfn software **[54]**, RDG scatter plots were generated. In addition, the 3D isosurfaces were visualized by the VMD software **[55]**. The study and calculation of thermodynamic parameters as well as the plots versus temperature were established using the Kisthelp 2019 program **[56]**.

3. Results and interpretation

3.1. *Structure description*

According to the results of the SC-XRD analysis, the F2NTh crystallized in a monoclinic system and belonged to the P21/c space group with four entities in the unit cell (Z = 4). The cell dimensions are given in **Table 1**. The title molecule is defined by its (E, Z) configuration, indicating the 3D distribution of the bonds and groups in the compound. The 3D-X-ray structure of the title compound as well as the optimized structure are shown in **Fig. 1. (a)** and **(b)**, respectively. The X-ray and computed geometrical parameters (bond lengths, bond angles, and dihedral angles) for non-hydrogen atoms are reported in **Table 2**. As can be seen in **Table 2**, experimental and theoretical results are consistent; note that the CAM-B3LYP functional gives a slightly closer result to the X-ray outcomes than the B3LYP **[57]**. It can clearly be observed that experimental and theoretically established S−C bond values are quite close and correspond to the reported values in the literature **[58]**. Whereas we noticed S1−C10 [1.750 (3) Å (X-ray), 1.766 Å (B3LYP), and 1.760 Å (CAM-B3LYP)]. Due to the conjugation of our molecule, we noted that the experimental and theoretical C=N double bond length is significantly shorter compared to the C–N single bond length. An average value of 1.42 Å for C–N was obtained for both X-rays and the two functionals, which is in good accordance with the reference value **[59]**. The bond length of O3=C11 was found to be 1.21 Å according to X-rays diffraction and 1.20 Å according to the theoretical calculation methods (B3LYP and CAM-B3LYP). The result turns out to be rather close to the value mentioned in the literature (1.22 Å) **[60]**. The C–C bond length in the fluoro-phenyls is in the range of [1.37−1.39 Å], which is slightly smaller than the given value in previous works **[61]**. From the C–C bond length of the previous aromatic rings (para-fluoro-phenyls), we noted that these latter are not perfect hexagons; similar works have supposed that the fluorine substitution, especially in the para position, is the cause of this phenomenon **[62]**. In our case, we can confirm this proposal by the fact that the two fluorine atoms of the title molecule participate in intermolecular interactions with the hydrogen atoms (C24–H24…F1 = 2.60 Å and C17–H17…F2 = 2.63 Å). These interactions have a direct effect on the lengths of the adjacent C–C bonds belonging to phenyl rings through repulsion and steric gene effect. For the F–C bond lengths, the common value cited in the literature is 1.36 Å **[63]**. This value is greater than the theoretical values for F1–C16 and F2–C22 (1.352 Å and 1.349 Å, respectively, at B3LYP) and (1.346 Å and 1.342 Å respectively at CAM-B3LYP). On the other hand, the corresponding experimental values for the two previous bonds are 1.347 (2) Å and 1.332 (2) Å, respectively.

The C–C–C bond angles within the phenyl rings were in the range of [120º (X-ray); 119º to 120º (for both B3LYP and CAM-B3LYP)], a finding that is almost identical to that reported values in the literature (120°) **[64]**. A deviation from the normal sp^2 hybridization angle was observed for the C–N–C bond angles, possibly due to the presence of the non-bonding nitrogen doublet **[65]**. The corresponding values that we obtained for C–N–C were [119.51º (15) (X-ray), 119.022º (B3LYP), and 119.571º (CAM-B3LYP)].

Torsion angles linking the four segments of the molecule allow us to interpret and compare the planarity in relation to each other. For example, the dihedral angle for C8–C9–C10–S1 was equal to 6.1º, C5–C6–C7–C8 (- 29.4º), C12–N3–C13–C14 (- 68.6º), and C12–N2–C19–C20 (78.4º). These values show that the nitro-phenyl and the thiazole ring are considerably deviated from each other, while the fluoro-phenyls are practically perpendicular to the thiazole ring. However, the allylidene moiety remains the closest group to the thiazole plan. In fact, the R^2 correlation values obtained by the B3LYP and CAM-B3LYP functionals are (0.988, 0.971, and 0.997) for the B3LYP and (0.985, 0.980, and 0.999) for the CAM-B3LYP level, corresponding to bond lengths, bond angles, and dihedral angles, respectively. These plots confirmed the good consistency of computed and experimental results and demonstrated that, as shown in **Fig. 2**, the results generated by CAM-B3LYP for geometric parameters are closer to experimental ones than the B3LYP level. We can summarize that our results are reasonably close and pleasing compared to similar studies carried out and published before **[66]**.

Table 2
Selected geometrical parameters by SC-XRD and DFT for F2NTh.

Bond lengths (Å)	X-ray	6-311G(d, p)	
		B3LYP	CAM-B3LYP
S1–C10	1.750(3)	1.766	1.760
S1–C12	1.775(3)	1.809	1.792
N1–O2	1.223(4)	1.223	1.214
N1–O1	1.223(3)	1.225	1.216
N1–C1	1.437(3)	1.481	1.475
F1–C16	1.347(2)	1.352	1.346
O3-C11	1.213(3)	1.209	1.203
N2–C11	1.379(4)	1.403	1.394
N2–C12	1.397(3)	1.395	1.392
N3–C12	1.258(4)	1.262	1.255
N3–C13	1.432(3)	1.407	1.408
F2–C22	1.332(2)	1.349	1.342
C13–C18	1.3732(12)	1.401	1.393
C14–C15	1.3732(12)	1.392	1.386

C7–C8	1.343(4)	1.351	1.338
C7–C6	1.488(3)	1.464	1.468
C8–C9	1.438(4)	1.436	1.442
C19–C20	1.3755	1.392	1.386
C23–C24	1.3756	1.390	1.384
C1–C2	1.3922	1.392	1.385
C1–C6	1.3922	1.411	1.401
Bond angles (º)	X-ray	B3LYP	CAM-B3LYP
C10–S1–C12	91.44(13)	091.21	091.19
O2–N1–O1	123.2(3)	124.49	124.59
O2–N1–C1	117.9(3)	117.30	117.34
O1–N1–C1	119.0(2)	118.20	118.06
C11–N2–C19	121.5(2)	121.10	121.25
C14–C13–C18	120.0	119.03	119.30
C14–C13–N3	120.38(15)	121.81	121.04
C15–C14–C13	120.0	120.56	120.47
C14–C15–C16	120.0	118.99	118.93
F1–C16–C17	120.13(14)	119.08	119.05
C17–C18–C13	120.0	120.66	120.51
N3–C12–S1	126.2(2)	126.55	126.11
C20–C19–C24	120.0	121.88	120.51
C19–C20–C21	120.0	119.96	119.94
C22–C21–C20	120.0	118.77	118.71
F2–C22–C23	120.03(12)	118.90	118.87
C21–C22–C23	120.0	122.13	122.18
C2–C1–C6	120.0	122.51	122.65
C2–C1–N1	116.93(13)	115.68	115.87
C3–C2–C1	120.0	119.89	119.69
Dihedral angles (º)	X-ray	B3LYP	CAM-B3LYP
C12–N3–C13–C14	−68.6(3)	−64.063	−73.12
N3–C13–C14–C15	−176.3(2)	−176.91	−177.58
C13–C14–C15–C16	0.00	0.013	0.11
C14–C15–C16–F1	179.8(2)	−179.88	−179.94
F1–C16–C17–C18	−179.8(2)	−179.57	−179.72
N3–C13–C18–C17	176.3(2)	177.59	177.98
C8C9–C10–C11	−176.7(3)	179.64	179.73
C8–C9–C10–S1	6.1(4)	−0.30	−0.26
C12–S1–C10–C9	173.8(3)	179.10	179.11
C12–N2–C11–O3	−176.9(3)	179.60	179.29
C19–N2–C11–C10	177.1(2)	−179.82	−179.68
S1–C10–C11–O3	−178.9(2)	−179.10	−178.84
C9–C10–C11–N2	−176.3(3)	−179.13	−179.04
C13–N3–C12–N2	177.1(2)	177.15	178.11
C13–N3–C12–S1	−4.7(4)	−4.39	−2.98
C19–N2–C12–S1	−179.91(16)	179.18	179.01
C10–S1–C12–N3	−173.1(3)	−177.97	−178.42
N2–C19–C20–C21	178.42(12)	179.30	179.42
F2–C22–C23–C24	178.68(13)	−179.84	−179.81
C21–C22–C23–C24	0.00	−179.71	0.37
N2–C19–C24–C23	−178.42(12)	−178.84	−178.91
O2–N1–C1–C6	155.5(2)	156.92	157.75
O1–N1–C1–C6	−25.9(3)	−24.10	−23.12
C6–C1–C2–C3	0.00	0.87	0.68
C4–C5–C6C7	−179.60(14)	−178.39	−178.81
N1–C1–C6–C5	176.56(19)	178.71	178.96
C2–C1–C6–C7	179.58(15)	177.16	178.96

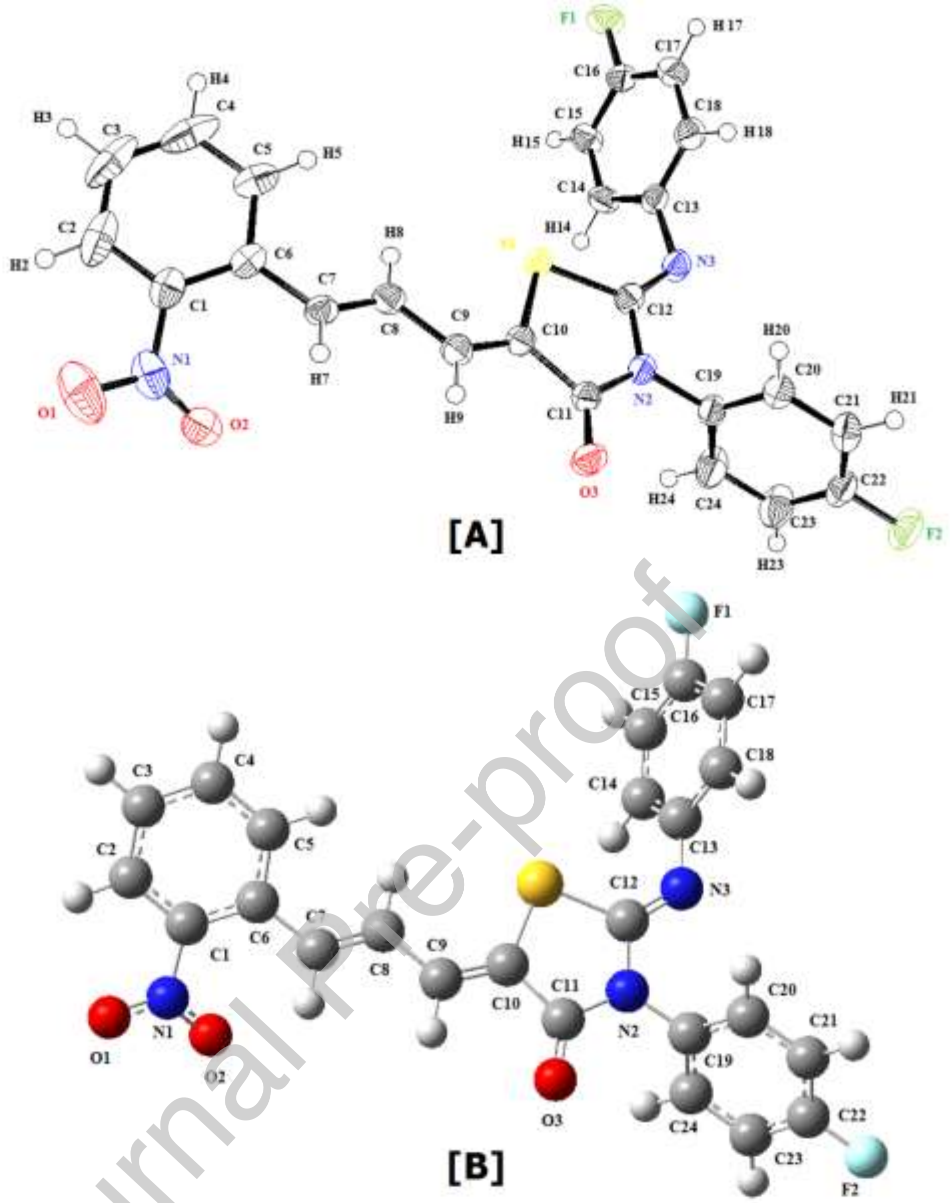

Fig. 1. 3D structure of F2NTh **[A]** by SC-XRD, and **[B]** calculated using B3LYP/6-311G(d,p).

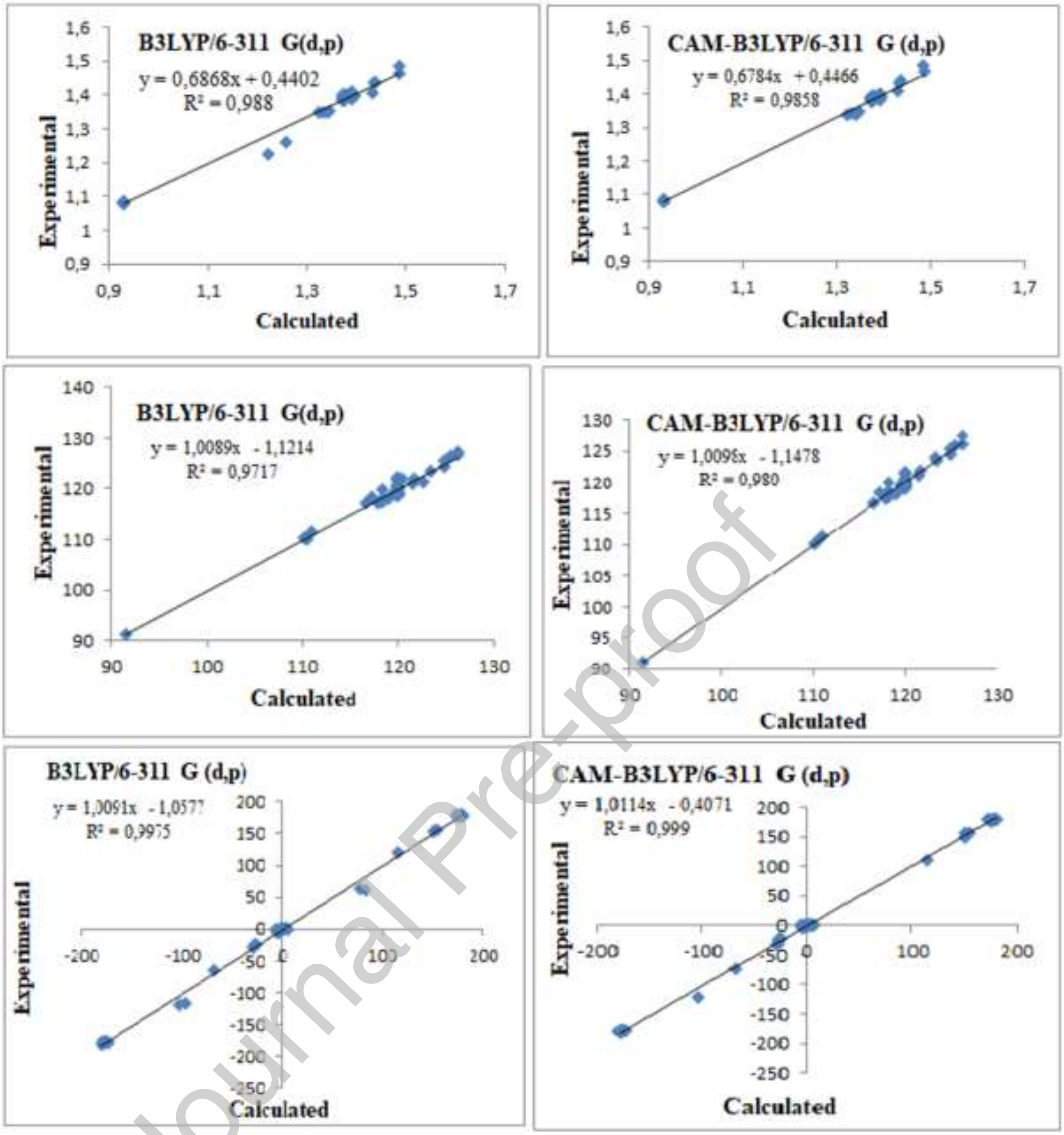

Fig. 2. Correlation plots of experimental and computed geometrical parameters for F2NTh.

3.2. **IR and NMR spectroscopy**

3.2.1. IR spectral analysis

Infrared spectroscopy is an efficient approach for the determination of functional groups in organic molecules. The title molecule was characterized by Fourier transform infrared (FT-IR) spectroscopy, and the theoretical vibrational frequencies were estimated. The F2NTh molecule has 104 vibration modes. The computed vibrational assignments of the standard modes were carried out on the basis of the potential energy distribution (PED) and presented in **Table 3**. The theoretical frequency values are considerably higher than the experimental ones. In this context, the errors have been reduced by the scaling factor of 0.967 for the B3LYP/6-311G (d,p) level of theory. The theoretical and experimental FT-IR spectra obtained were overlaid for a better comparison and are given in **Fig. 3**. The B3LYP functional seems to have given more similar results to the experimental spectrum than those established by CAM-B3LYP **[67]**. Due to this rationale, we have exclusively presented the theoretical outcomes achieved at the B3LYP level.

3.2.1.1. Aromatic ring vibrations

The literature has shown that absorption of aromatic C-H stretching mode is typically anticipated in the region of 3000–3100 cm^{-1} **[68, 69]**, which is approximately consistent with our results, that are around 2840 cm^{-1} experimentally and 3085 cm^{-1} theoretically. The carbon-carbon stretching vibrations were determined experimentally and through B3LYP/6-311G (d, p) calculations. The observed C-C stretching vibrations in the FT-IR spectrum appeared at 1121, 1295, 1571, and 1633 cm^{-1}, while the calculated values were 1088, 1262, 1554, and 1589 cm^{-1}. The CCC in-plane bending bands were observed in the IR spectrum at 646 and 695 cm^{-1}, which closely matched the calculated values of 632 and 678 cm^{-1} with intensities of 30% and 22%, respectively. These findings are in excellent accordance with previously published research **[70]**.

3.2.1.2. *Nitro group vibrations*

Asymmetric stretching vibrations of substituted nitrobenzene occur in the range of 1380-1560 cm^{-1} **[71]**. In the FT-IR spectra of the titled compound, a distinct peak at 1343 cm^{-1} is observed, which is assigned to the asymmetric stretching vibrations of the NO_2 group. This value closely corresponds to the B3LYP/6-311 G (d, p) level calculation result of 1311 cm^{-1}. Additionally, the anticipated N-C stretching vibration between the nitrogen of the nitro group and the carbon of aromatic ring 1 was predicted to be 1092 cm^{-1} through B3LYP calculation, and it was found to be 1063 cm-1 in the FT-IR spectrum.

3.2.1.3. *Carbon–oxygen vibrations*

Depending on the type of stereoisomerism of the molecule, (C=O) stretching frequencies are commonly observed in the field of 1600-1800 cm^{-1} **[72]**. A strong band was identified at 1721 cm^{-1} in the experimental spectrum as carbonyl (C=O) stretching vibration, corresponding to the calculated one at the B3LYP level with a value of 1698 cm^{-1} and 73% PED.

3.2.1.4. *Carbon–sulfur vibrations*

The single bond C–S stretching vibration of the thiazole ring is reported in the literature **[73]** in the region of 500-700 cm^{-1}. This agrees well with the obtained peak in the FT-IR spectrum at 506 cm^{-1}, as well as the calculated value by B3LYP/6-311 G(d, p) level at 477 cm^{-1}. Additional vibration modes have been found corresponding to out-of plan bending, which have values of 436 and 469 cm^{-1}. These have been assigned to asymmetric and symmetric out-of-plan bending, calculated by the B3LYP level of theory. On the other hand, the observed values in the FT-IR spectrum are 427 and 466 cm^{-1}.

3.2.1.5. *Carbon–Nitrogen vibrations*

Usually, the vibrational modes in the region of 1640−1690 cm^{-1} are referred to as stretching vibration bands of the imine group (C=N) **[74]**. In the current section, C=N stretching vibrations (linked to the thiazole ring) were identified in the middle region of the FT-IR spectrum at 1681 cm^{-1} and reported at 1639 cm^{-1} by the B3LYP level. It may also be discerned from our experimental results that an asymmetric stretching vibration band of C–N belonging to the thiazole ring is obtained at an average of 1370 cm^{-1} and reported theoretically at 1325 cm^{-1}. The out-of-plan and twisting mode vibrations of the C–N attached to the thiazole ring were noticed at 581 and 599 cm^{-1} as asymmetric vibrations at the B3LYP level and the FT-IR spectrum, respectively.

3.2.1.6. *Carbon-Fluorine vibrations*

The aromatic C–F stretching vibrations are anticipated to be in the region of 1000-1400 cm^{-1} **[75]**. According to the calculation performed by B3LYP level, the stretching vibration of C–F has a value corresponding to 1220 cm^{-1} with a 46% PED; this value fits to 1214 cm^{-1} in the FT-IR spectrum and fits well with the above-mentioned interval.

Table 3
Experimental and calculated wavenumbers (cm^{-1}) of F2NTh.

Mode	FT-IR	B3LYP/6-311G (d, p)			Assignments with PED (≥10 %)
		Unscaled	Scaled	I_{IR}	
104		3211	3124	2.44	υ_s CH (96%) $_{\text{(ring 1)}}$
103		3200	3114	0.68	υ_s CH (94%) $_{\text{(ring 3)}}$
102		3198	3112	0.92	υ_s CH (94%) $_{\text{(ring 3)}}$
101		3189	3103	4.25	υ_s CH (88%) $_{\text{(ring 2)}}$
100		3187	3101	2.62	υ_s CH (88%) $_{\text{(ring 2)}}$
99		3186	3100	3.78	υ_s CH (40%) + υ_s CH (49%) $_{\text{(ring 1)}}$
98		3185	3099	0.15	υ_{as} CH (40%) $_{\text{(ring 3)}}$ + υ_s CH (59%) $_{\text{(ring 3)}}$
97		3185	3099	9.03	δ_s HCC (59%) $_{\text{(ring 2)}}$ + υ_{as} CH (32%) $_{\text{(ring 1)}}$
96		3184	3098	10.60	υ_{as} CH (32%) $_{\text{(ring 1)}}$ + υ_s CH (62%) $_{\text{(ring 1)}}$
95		3178	3092	6.50	υ_{as} CH (65%) $_{\text{(ring 3)}}$ + υ_s CH (34%) $_{\text{(ring 3)}}$
94		3173	3087	2.17	υ_{as} CH (33%) $_{\text{(ring 2)}}$ + υ_s CH (65%) $_{\text{(ring 2)}}$
93	2840	3171	3085	9.48	υ_{as} CH (21%) $_{\text{(ring 2)}}$ + υ_s CH (65%) $_{\text{(ring 2)}}$
92	2755	3162	3077	2.00	$\upsilon_{as\ CH}$ (30%) $_{\text{(ring 1)}}$ + υ_{CH} (70%) $_{\text{(ring 1)}}$
91		3148	3063	1.83	υ_s C9H9 (92%)

90		3130	3045	4.53	υ_{s} C8H8 (91%)
89	1721	1745	1698	130.77	υ_{s} OC (73%) $_{(thiazol)}$ + υ_{s} NC $_{(thiazol)}$ (10%)
88	1682	1684	1639	915.11	υ_{s} NC $_{(thiazol)}$ (68%)
87		1647	1603	66.22	υ_{s} C7C8 (28%) + υ_{s} CC (10%) $_{(ring\ 1)}$
86		1642	1598	38.25	υ_{as} CC (11%) $_{(ring\ 3)}$ + υ_{s} CC (38%) $_{(ring\ 3)}$
85		1638	1594	27.54	υ_{s} CC (36%) $_{(ring\ 2)}$
84	1633	1633	1589	46.89	υ_{as} C7C8 (22%) + υ_{s} CC (14%) $_{(ring\ 1)}$
83		1628	1584	9.39	υ_{as} CC (29%) $_{(ring\ 3)}$ + υ_{s} CC (23%) $_{(ring\ 3)}$
82		1622	1578	69.37	υ_{s} CC $_{(thiazol)}$ (53%)
81		1611	1568	6.15	υ_{as} CC (17%) $_{(ring\ 2)}$ + υ_{s} CC (34%) $_{(ring\ 2)}$
80	1571	1597	1554	250.89	υ_{as} CC (21%) $_{(ring\ 1)}$ + υ_{s} CC (23%) $_{(ring\ 1)}$ + δ_{s} HCC (11%) $_{(ring\ 1)}$
79		1554	1512	250.89	υ_{as} O1N1 (37%) + υ_{s} O2N1 (36%)
78		1538	1496	257.13	δ_{s} HCC (32%) $_{(ring\ 3)}$ + δ_{as} HCC (27%) $_{(ring\ 3)}$ + δ_{s} CCC (10%) $_{(ring\ 3)}$
77		1530	1489	233.48	δ_{as} HCC (33%) $_{(ring\ 2)}$ + δ_{s} HCC (24%) $_{(ring\ 2)}$
76	1499	1500	1460	4.5889	δ_{s} HCC (51) $_{(ring\ 1)}$
75		1468	1446	13.12	υ_{as} CC (13%) $_{(ring\ 1)}$ + δ_{as} HCC (36%)$_{(ring\ 1)}$ + δ_{s} HCC (19%) $_{(ring\ 1)}$
74		1442	1403	0.41	υ_{as} CC (21%) $_{(ring\ 3)}$ + υ_{s} CC (20%) $_{(ring\ 3)}$
73	1436	1435	1396	3.62	υ_{as} CC (23%) $_{(ring\ 2)}$ + υ_{s} CC (24%) $_{(ring\ 2)}$
72	1418	1371	1334	226.15	δ_{as} H9C9C8 (10%) + δ_{s} HCC (29%) $_{(ring\ 1)}$
71	1369	1362	1325	389.15	υ_{as} NC (20%) $_{(thiazol)}$ + υ_{s} NC (23%) $_{(thiazol)}$ + δ_{s} HCC (12%) $_{(ring\ 1)}$
72	1343	1348	1311	174.83	υ_{as} O1N1 (52%) + δH8C8C7 (11%) + δ_{s} O2N1O1 (10%)
69		1339	1303	30.88	υ_{s} C7C8 (15%) + δ_{s} H8C8C7 (26%) + δ_{as} HCC (12%) $_{(ring\ 1)}$
68		1326	1290	100.47	υ_{as} CC (10%) $_{(ring\ 1)}$ + υ_{s} CC (16%) $_{(ring\ 1)}$ + δ_{s} H8C8C7 (12%) + δ_{s}HCC (13%) $_{(ring\ 1)}$
67		1324	1288	12.32	υ_{s} CC (21%) $_{(ring\ 3)}$ + δ_{as} HCC (12%) $_{(ring\ 3)}$ + δ_{s} HCC (12%) $_{(ring\ 3)}$
66		1313	1278	3.02	υ_{s} CC (22%) $_{(ring\ 3)}$ + δ_{as} HCC (16%) $_{(ring\ 3)}$ + δ_{s} HCC (14%) $_{(ring\ 3)}$
65	1314	1312	1277	3.08	δ_{as} HCC (44%) $_{(ring\ 2)}$ + δ_{s} HCC (39%) $_{(ring\ 2)}$
64		1301	1266	72.17	υ_{as} CC (16%) $_{(ring\ 1)}$ + δH9C9C8 (24%) + δ_{s} HCC (10%) $_{(ring\ 1)}$
63	1295	1297	1262	1.46	υ_{as} CC (37%) $_{(ring\ 2)}$ + υ_{s} CC (48%) $_{(ring\ 2)}$
62		1288	1253	53.64	υ_{as} NC (13%) $_{(thiazol)}$ + υ_{s} NC (22%) $_{(thiazol)}$
61	1272	1280	1245	26.47	υ_{s} CC (12%) $_{(ring\ 1)}$ + δ_{s} H8C8C7 (15%)
60		1259	1225	285.66	υ_{as} CC (10%) $_{(ring\ 3)}$ + υ_{s} FC (48%) $_{(ring\ 3)}$
59	1214	1254	1220	111.15	υ_{s} FC (46%) $_{(ring\ 2)}$ + δ_{as} HCC (11%) $_{(ring\ 2)}$
58		1236	1203	3.42	υ_{as} CC (11%) $_{(ring\ 1)}$ + υ_{as} CC (13%) $_{(ring\ 1)}$ + υ_{s} CC (19%) $_{(ring\ 1)}$ + δ_{s} HCC (10%)$_{(ring\ 1)}$
57		1198	1166	134.55	υ_{s} C8C9 (17%)
56	1184	1188	1156	44.45	δ_{as} HCC (17%) $_{(ring\ 1)}$ + δ_{s} HCC (52%) $_{(ring\ 1)}$
55		1178	1146	66.83	υ_{s} C8C9 (14%) + δ_{s} HCC (24%) $_{(ring\ 3)}$
54		1174	1142	186.29	δ_{s} HCC (56%) $_{(ring\ 3)}$
53		1172	1140	89.83	δ_{s} HCC (65%) $_{(ring\ 2)}$
52		1157	1126	105.94	υ_{s} CC (11%) $_{(ring\ 1)}$ + υ_{s} NC (12%) $_{(thiazol)}$
51	1149	1153	1122	73.82	υ_{NC} (12%) $_{(thiazol)}$
50	1120	1118	1088	12.41	υ_{as} CC (12%) $_{(ring\ 3)}$ + υ_{s} CC (14%) $_{(ring\ 3)}$ + δ_{as} HCC (33%) $_{(ring\ 3)}$ + δ_{s} HCC (30%) $_{(ring\ 3)}$
49		1115	1085	11.01	υ_{as} CC (12%) $_{(ring\ 2)}$ + υ_{s} CC (13%) $_{(ring\ 2)}$ + δ_{as} HCC (30%) $_{(ring\ 2)}$ + δ_{s} HCC (38%) $_{(ring\ 2)}$
48	1092	1093	1063	8.10	υ_{as} NC (12) $_{(ring\ 1)}$ + δ_{as} HCC (14) $_{(ring\ 1)}$ + δ_{s} CCC (20) $_{(ring\ 1)}$
47		1067	1038	3.50	υ_{s} CC (22%) $_{(ring\ 1)}$
46		1062	1033	36.02	υ_{s} CC (13%) $_{(ring\ 1)}$ + υsCC (17%) $_{(thiazol)}$
45		1029	1001	6.27	δ_{s} CCC (15%) $_{(ring\ 3)}$ + δ_{as} CCC (58%) $_{(ring\ 3)}$
44		1023	995	2.99	δ_{s} CCC (70%) $_{(ring\ 2)}$ + δ_{as} CCC (16%) $_{(ring\ 2)}$
43	1012	1015	988	3.21	τ_{s} HCCC (54%) $_{(ring\ 1)}$ + τ_{as} CCCC (16%) $_{(thiazol)}$
42		1002	975	42.24	τ_{s} HCCC (39%) $_{(ring\ 1)}$ + τ_{as} HCCC (32%) $_{(ring\ 1)}$ + τ_{as} HCCC

					(12%) (thiazol)
41	991	990	963	1.37	τ_{as} HCCC (37%) (ring 1) + τ_s HCCC (55%) (ring 1)
40	976	968	942	0.36	τ_s HCCC (73%) (ring 2)
39		967	941	0.12	τ_{as} HCCC (53%) (ring 3) + τ_s HCCC (20%) (ring 3)
38		948	922	1.93	τ_{as} HCCC (20%) (ring 3) + τ_s HCCC (50%) (ring 3)
37		947	921	2.27	τ_{as} HCCC (36%) (ring2) + τ_s HCCC (12%) (ring 2) + τ_{as} CCCC (27%) (ring 2)
36	934	941	916	0.41	τ_{as} HCCC (64%) (thiazol) + τ_s HCCC (23%) (ring 1)
35	899	913	888	0.77	τ_{as} HCCC (11%) (ring 1) + τ_s HCCC (54%) (ring 1)
34	880	879	855	6.72	τ_{as} H8C8C7C6 (15%) +τ_{as} HCCC (35%) (ring 1)
33		877	853	27.62	δ_s ONO (20%)
32	863	858	835	38.33	τ_{as} HCCC (17%) (ring 3) + γ_{as} FCCC (10%) (ring 3)
31		855	832	20.89	τ_{as} HCCC (29%) (ring 2) + τ_s HCCC (28%) (ring 2) + γ_{as} FCCC (10%) (ring 2)
30		848	825	46.06	δ_s O2N1O1 (23%) + δ_s CCC (10%) (ring 1)
29	828	827	805	1.58	τ_{as} HCCC (24%) (ring 1) + τ_{as} HCCC (20%) (ring 2) + τ_s HCCC (53%) (ring 2)
28		822	780	4.81	τ_{as} HCCC (29%) (ring 3) + τ_s HCCC (55%) (ring 3)
27	800	819	797	42.68	δ_{as} OCC (10%) (thiazol) + τ_s HCCC (13%) (ring 3)
26		804	782	14.98	τ_{as} HCCC (32%) (ring 1) + τ_s HCCC (19%) (ring 1) + γ_s OCON (27%) (ring 1)
25	786	800	778	5.22	υ_s FC (14%) (ring 3) + υ_{as} CCC (11%) (ring 3)
24		765	744	15.29	τ_s HCCC (23%) (ring 1) + γ_{as} OCON (20%) (ring 1)
23	751	755	735	24.20	γ_{as} ONCC (68%) (thiazol)
22	735	727	707	2.15	τ_{as} CCCC (52%) (ring 2) + τ_s CCCC (12%) (ring 2)
21	718	718	699	16.02	τ_{as} CCCC (10%) (ring 1) +τ_{as} OCON (13%) (ring 1)
20	707	715	696	8.49	τ_{as} CCCC (21%) (ring 1) + τCCCC (14%) (ring 3)
19	695	697	678	2.44	δ_{as} O2N1O1 (11%) + δ_s CCC (22%) (ring 1)
18	674	661	643	10.65	δ_{as} CCC (11%) (ring 2)
17		656	638	8.19	δ_s CCC (10%) (ring 2)
16	646	650	632	0.40	δ_{as} CCC (30%) (ring 3) + δ_s CNC (26%) (thiazol)
15		625	608	2.34	δ_s CNC (12%) (thiazol)
14	610	611	595	4.76	τ_s NCNC (15%) (thiazol)
13	599	597	581	4.47	τ_{as} NCNC (41%) (thiazol) + γ_{as} CCCN (11%) (thiazol)
12		574	559	3.07	δ_s ONC (18%) (ring 1) + δ_s CCC (10%) (ring 1)
11		552	537	80.59	δ_s CCN (16%) (thiazol)
10	543	540	525	36.51	τ_{as} HCCC (11%) (ring 3) + γ_s FCCC (23%) (ring 3) + γ_{as} NCCC (14%) (ring 3)
09	532	522	508	11.48	τ_{as} CCCC (28%) (ring 2)
08	505	490	477	5.70	υ_s SC (23%) (thiazol) + δ_s OCC (10%) (thiazol)
07	469	479	466	8.60	γ_s SCCC (14%) (thiazol)
06		448	436	4.95	υ_{as} FCC (10%) (ring 2)
05	436	439	427	0.73	δ_{as} NCC (11%) (ring 3) + δ_s FCC (23%) (ring 3) + γ_{as} SCCC (11%) (ring 3)
04		433	421	0.61	τ_{as} HCCC (20%) (ring 3) +τ_{as} CCCC (15%) (ring 3) + τ_s CCCC (54%) (ring 3)
03		432	420	1.87	τ_s CCCC (44%) (ring 2)
02		425	414	12.93	δ_{as} ONC (12%) (ring 1)
01		405	394	0.13	υ_s NC (19%) (ring 1) + δ_s CCC (10%) (ring 1)

ν: stretching; **s:** symmetric; **as:** asymmetric; **γ :** out of plan; **τ:** twisting; **δ:** bending. **Ring 1:** C1/C6; **ring 2**: C13/C18, **ring 3:** C19/C24.

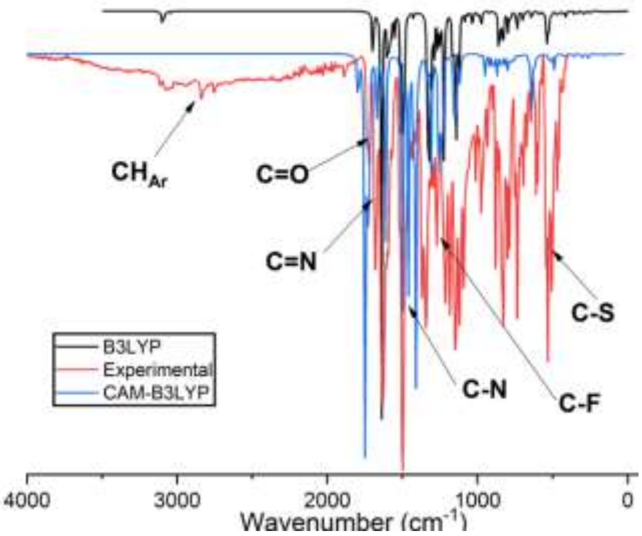

Fig. 3. Experimental and theoretical IR spectra of F2NTh.

3.2.2. ^{1}H and ^{13}C NMR chemical shifts

It is known that NMR crystallography combines both theory and experiment to obtain previously inaccessible information on the structure and behavior of organic molecules. This combination of experimental and calculated chemical shifts for a structural model is used to confirm the crystal structure **[76]**. The ^{13}C and ^{1}H NMR chemical shifts of the title compound were predicted using the Gauge-Inclusive Atomic Orbital (GIAO) **[53]** at the B3LYP/6-311G (d,p) level of theory. **Table 4** provides calculated chemical shifts considering the tetramethylsilane (TMS) alongside the experimental results as a reference, with chemical shielding at 32.50 ppm (^{1}H) and 184.48 ppm (^{13}C) for B3LYP/6-311G (d,p). As anticipated, the ^{13}C NMR chemical shifts were found to vary in the range of 122 to 171 ppm. For the first benzene ring carbons (ring 1), the carbons C2, C3, and C5 have close chemical shifts ranging between 130.02 and 131.27 ppm for the experimental spectrum and from 132.66 to 135.61 ppm for the theoretical calculations. This could probably be due to their similar molecular environment. On the other hand, the chemical shift of the C1 linked directly to the electron-attractant NO_2 group with both an inductive and mesomeric effect is more important, having an experimental value of 158.44 ppm and a theoretical value of 156.82 ppm. The carbon C4 of the same ring has a chemical shift from the experimental spectrum of 143.89 ppm to a theoretical value of 140.83 ppm. This high value compared to the rest of the carbons constituting ring 1 can be explained by the hydrogen bonding formed between C4–H4 and oxygen O3 (C4–H4…O3), thus increasing the polarity of this bond and varying the polarization of the carbon C4. Regarding the NMR results of the thiazole ring, the two carbons C11 and C12 of the ring have high chemical shift values due to their proximity to the heteroatoms of the ring (nitrogen and oxygen), with a chemical shift for C11 in the average of 170.58 and 170.71 ppm for the experimental and theoretical spectra, respectively. For C12, the experimental and theoretical shifts are 161.56 and 157.27 ppm, respectively. It should be noted that the experimental and theoretical shifts of C11 are largely higher than those of C12 because the linked oxygen atom O3 to C11 acts as a nucleophile and strongly participates in the intermolecular interactions of the title molecule, thus polarizing the bond and increasing the shift of the carbon C11. This statement will be soon confirmed in the MEP analysis, atomic charges, and Fukui functions sections, where we will study more precisely the nucleophilic and electrophilic behavior of F2NTh atoms and be able to relate them to NMR results. We can also explain the reason that makes the theoretical values slightly different from the experimental ones by the fact that the molecule is in its isolated state in the gas phase. For the three carbons (C7, C8, and C9) of the allylidene bridge, we found chemical shift values within the norms of the literature **[37]**, except for carbon C7 (δ = 147.34 ppm for experimental and δ = 148.00 ppm for theoretical shift), which has a higher shift than the others due to its close position to the nitrophenyl ring. In the two remaining fluoro-phenyl rings (ring 2 and ring 3), we found the same behavior and chemical shifts of the carbons constituting these two rings due to their similar structure, except for the two carbon atoms linked to the fluorine ones: C16 (δ = 169.71 ppm for experimental and δ = 169.57 ppm for theoretical shift) and C22. **Table 4** shows that C22 holds the highest experimental and theoretical chemical shifts (δ_{exp} = 171.32 ppm and δ_{theo} = 172.33 ppm). These significant values are due to the direct connection of the considered atom with the F1 atom, which is more active in the molecule than the F2 atom. This reactivity is due to the involvement of the F1 atom in the intermolecular interactions compared to the F2 atom.

Regarding the ^{1}H NMR results, the chemical shifts of the aromatic ring protons are in good agreement with those previously published **[59, 69]**, where the observed values in the experimental spectrum ranged from 6.64 to 9.80 ppm and those established by B3LYP/6-311G (d, p) ranged from 7.31 to 8.70 ppm.

Table 4

Experimental and calculated ^{1}H and ^{13}C-NMR isotropic chemical shifts (ppm) using B3LYP/6-311G (d,p) for F2NTh

Atoms	Chemical shifts		Atoms	Chemical shifts	
^{13}C	Experimental	Theoretical	^{1}H	Experimental	Theoretical
C1	158.44	156.82	H2	9.80	8.70
C2	130.02	132.66	H3	7.95	7.98
C3	131.27	135.51	H4	8.02	8.18
C4	143.89	140.89	H5	8.03	8.22
C5	131.16	134.80	H7	8.01	8.10
C6	143.86	140.33	H8	7.28	7.40
C7	147.34	148.00	H9	7.90	7.94
C8	130.44	133.39	H14	6.64	7.31
C9	135.47	137.53	H15	7.40	7.49
C10	132.64	135.61	H17	7.71	7.60
C11	170.58	170.71	H18	7.03	7.51
C12	161.66	157.25	H20	7.98	8.04
C13	155.55	152.11	H21	7.80	7.66
C14	127.49	126.00	H23	8.75	7.66
C15	122.44	121.21	H24	7.85	7.87
C16	169.71	169.57			
C17	122.56	121.95			
C18	129.95	129.69			
C19	136.46	139.01			
C20	133.85	137.44			
C21	122.25	121.02			
C22	171.32	172.33			
C23	122.35	121.13			
C24	133.32	136.79			

3.3. **UV-Visible spectral analysis**

The absorption or emission of radiation by organic molecules is the key to the interpretation of charge transfer phenomena within the molecule. Using the TD-DFT method with the B3LYP and CAM-B3LYP functionals, some properties of the excited states occurring in the F2NTh molecule were determined. The experimental UV spectrum of the title compound was measured in the region of 200-600 nm using chloroform as a solvent. According to the literature, the CAM-B3LYP calculation functional would be a correction of B3LYP for a more reliable result and for the study of certain parameters and could lead to theoretical spectra that are more aligned with experimental ones **[77]**. Among these parameters is the UV-visible analysis, which can be clearly observed in **Fig. 4** which represents the superposition of the three UV spectra: B3LYP, CAM-B3LYP, and the experimentally measured spectrum. In addition, vertical excitation energy, oscillator strength (*f*), transition wavelength (λ), and atomic orbital contributions were determined by TD-DFT using the B3LYP and CAM-B3LYP functionals and are collected in **Table 5**. It can be seen from **Fig. 4** that the experimental spectrum has two ultraviolet peaks at 270 and 365 nm; there are also two peaks for CAM-B3LYP that are slightly close to the experimental ones at 289 and 346 nm. On the other hand, for B3LYP, the two peaks appeared at 369 and 450 nm, also in the ultraviolet range and fairly close to the visible range. The computed results for oscillator factor strength and atomic orbital contributions for both B3LYP and CAM-B3LYP 6-311 G (d, p) levels were as follows: λ = 369 nm, *f* = 0.594 corresponding to HOMO-1→ LUMO (14%) and HOMO-2→LUMO+1 (83%); also λ = 450 nm, *f* = 0.511 corresponding to HOMO→LUMO (97%) for B3LYP. However, for CAM-B3LYP, reported results were λ = 289 nm, *f* = 1.189, corresponding to HOMO→LUMO+1 (67%) and λ = 346 nm**,** *f* = 0.097, corresponding to HOMO→LUMO (83%). The experimental bands measured at 270 and 365 nm have been assigned to n–π* and π–π* transitions. Finally, for the UV analysis, it can be stated that experimental results and those of the CAM-B3LYP calculation are in good agreement **[77]**.

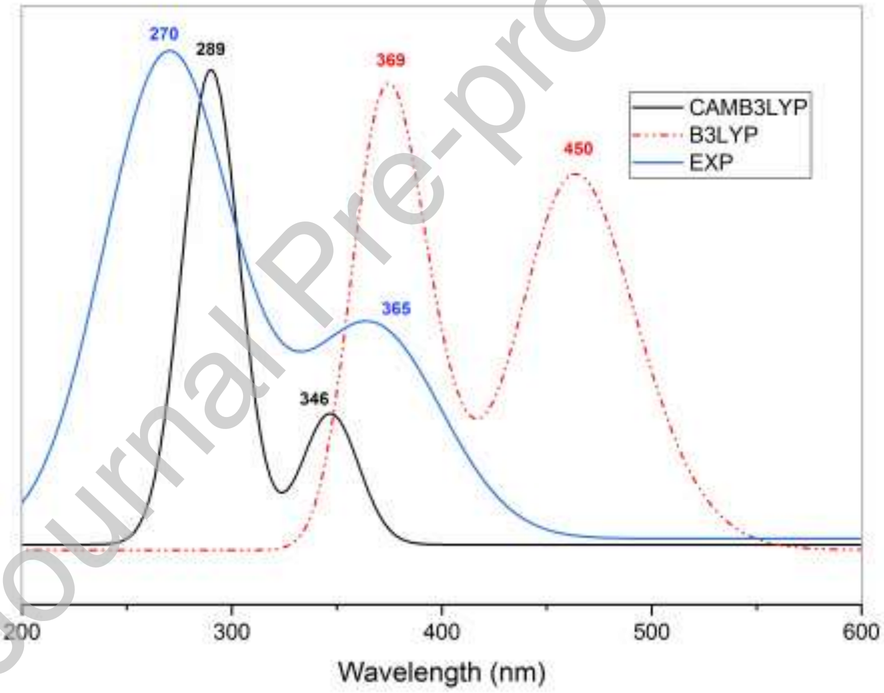

Fig. 4. Experimental and theoretical UV-Vis spectra for F2NTh.

Table 5

Electronic transitions computed by TD-DFT method (MO Contribution ≥ 10 %).

Electronic transitions	B3LYP				CAM-B3LYP			
	λ (nm)	Energy (eV)	Osc. Stren. (*f*)	MO Contributions	λ (nm)	Energy (eV)	Osc. Stren. (*f*)	MO Contributions
S0→S1	450.12	2.221	0.511	H→L (97%)	345.89	3.584	0.097	H→L (83%)
S0→S2	399.99	2.500	0.034	H-1→L (84%) H→L+1 (14%)	305.78	4.054	0.016	H-11→L (17%) H-11→L+1(17%) H-9→L (16%) H-9→L+1 (13%) H-6→L (13%)
S0→S3	368.71	2.712	0.594	H-1→L (14%) H-2→L+1 (83%)	288.76	4.293	1.189	H→L+1 (67%)
S0→S4	346.27	2.887	0.021	H-2→L (94%)	277.61	4.466	0.075	H-1→L (44%) H-1→L+1 (21%)
S0→S5	334.86	2.986	0.089	H-1→L+1 (87%)	270.78	4.578	0.002	H-13→L (24%) H-13→L+1(21%) H-11→L+1(10%)
S0→S6	325.91	3.068	0.029	H-9→L (25%) H-6→L (29%)	255.40	4.854	0.053	H-8→L (11%) H-7→L (10%) H-2→L (28%)
S0→S7	306.87	3.258	0.062	H-5→L (18%) H-4→L (12%) H-3→L (47%)	254.46	4.872	0.069	H-8→L (16%) H-2→L (32%) H-2→L+1(10%)
S0→S8	302.93	3.301	0.017	H-8→L (12%) H-7→L (10%) H-5→L (42%) H-4→L (13%)	249.07	4.978	0.086	H-6→L (51%)
S0→S9	298.94	3.345	0.001	H-4→L (40%) H-3→L (43%)	242.97	5.102	0.070	H-5→L (33%) H-3→L (13%)
S0→S10	296.45	3.373	0.008	H-2→L+1 (91%)	241.47	5.134	0.032	H-1→L+5 (17%) H→L+4 (15%)

3.4. **Hydrogen bonding, Hirshfeld surface and RDG analysis**

3.4.1. Hydrogen bonding

In recent decades, interest in studies of systems, including H-bonds, has increased **[78]**. Hydrogen bond donation plays a more prominent role. These bonds occur between a hydrogen atom and an electronegative atom, such as oxygen, fluorine, or nitrogen. Understanding hydrogen bonding helps researchers analyze the structure, stability, and reactivity of molecules, as well as their physical and chemical properties. The electron density of the molecules' heteroatoms influences the strength of hydrogen bonding connections between the constituent molecules. The C–F bond is recognized for its ability to serve as a hydrogen bond acceptor **[79]**. The nonlinear optical properties of materials can also be affected by hydrogen bonding. This phenomenon occurs due to the strong dipole-dipole interactions between hydrogen atoms and electronegative atoms. These interactions can enhance the material's ability to exhibit optical nonlinearity, making it useful in various applications such as optical switches and frequency converters **[80]**. Numerous hydrogen bonds are present in the title molecule, according to a supramolecular study. The most important H-bonds, present in the title compound are C4–H4…O3 and C17–H17…F1 with a bond length equal to 2.22 Å and 2.60 Å, respectively, in which the carbon (C) atom acts as a donor while oxygen (O) and fluorine (F) act as acceptors. The stability of the molecular packing in the unit cell is supported by these intermolecular interactions. As found in X-ray data, H-bonds occurring within the title compound are listed in **Table 6** and are shown in **Fig. 5**.

Table 6

Hydrogen bonds observed in the F2NTh by X-ray diffraction (Å, º)

D–H…A	D–H (Å)	H…A (Å)	D…A (Å)	D–H…A (º)	Symmetry
C24–H24…F1	0.93	2.60	3.492 (2)	160.7	-x+1, y-1/2, -z+1/2
C14–H14…N3	0.93	2.86	3.521 (3)	129.1	-x+1, y-1/2, -z+1/2
C17–H17…F1	0.93	2.60	3.372 (3)	141.0	-x+1, -y+1, -z
C17–H17…F2	0.93	2.63	3.442 (3)	146.3	x, -y+3/2, z-1/2
C7–H7…O3	0.93	2.78	3.489 (4)	133.6	-x, y-1/2, -z+1/2
C9–H9…O1	0.93	2.65	3.516 (4)	154.6	-x, y+1/2, -z+1/2
C20–H20…O1	0.93	2.78	3.474 (3)	132.6	x, y+1, z
C21–H21…O3	0.93	2.89	3.740 (3)	153.0	x, y+1, z
C21–H21…O2	0.93	2.65	3.043 (3)	105.8	-x, y+3/2
C20–H20…O2	0.93	2.77	3.103 (3)	102.3	-x, y+3/2
C24–H24…F1	0.93	2.97	3.623 (3)	128.5	x, -y+1/2, z+1/2
C4–H4…O3	0.93	2.22	3.078 (3)	152.4	x, -y-1/2
C5–H5…F2	0.93	2.78	3.517 (3)	136.8	x, -y+1/2, -1/2

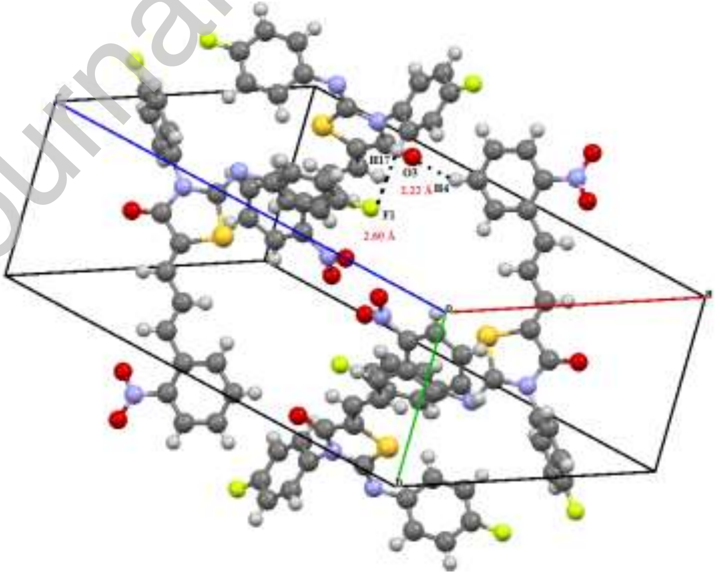

Fig. 5. Crystal packing of F2NTh in the unit cell.

3.4.2. Hirshfeld surface analysis

The Hirshfeld surface (HS) analysis provides surface features common to several kinds of interactions among molecules **[81]**. It constitutes an efficient tool for understanding the contribution that each intermolecular interaction generates **[82]**. The molecular HS in the crystal structure was established on the basis of the electron density distribution, calculated as the sum of the electron densities of spherical atoms **[83]**. A weight function W_a (r) offers a description of each atom from the framework of the theoretical description of the Hirshfeld surface:

$$w_a\,(r) = \rho_a^{at} / \sum_{molecule} \rho_a^{at}\,(r)$$

Where $\rho_a^{at}(r)$ represent the averaged spherical electron density of the respective atoms **[84]**. Dipole interactions via hydrogen bonds are crucial for stabilizing the structures, so according to these hydrogen bonds, the 2D fingerprint plot for the Hirshfeld isosurface indicates two distances for each point: d_e, which represents the distance from the point to the closest nucleus external to the surface, and d_i, which represents the distance from the closest nucleus internal to the surface **[85]**. The following equation describes the d_{norm} (normalized contact distance), which is determined from the d_e, d_i, and interior/exterior Vander Waals radii of atoms (r_i^{vdw} and r_e^{vdw}):

$$d_{norm} = \frac{d_i - r_i^{vdw}}{r_i^{vdw}} + \frac{d_e - r_e^{vdw}}{r_e^{vdw}}$$

The HS analysis, combined with the study of hydrogen bonding in thiazolidinone molecules, enables us to visualize and quantify the various intermolecular interactions on the total surface of the molecule. This leads us to a deeper understanding of the stability, structure, and energy implications occurring within the molecule. The HS analysis and 2D fingerprint plots are key tools for providing information on the nature of intermolecular interactions and the arrangement of molecules in the crystal structure **[86]**. Different regions of the HS represent specific types of interatomic interactions, such as hydrogen bonding, van der Waals interactions, and steric collisions. By analyzing these regions, we can gain an overview of the dominant forces that govern the arrangement and stability of molecules in the crystal lattice. 2D fingerprint diagrams allow the identification of the most important interactions and their contributions, including hydrogen bonds and close van der Waals contacts. For interpreting HS, a color system is used; the latter enables us to state that when established contact is shorter than the Vander Waals radii, the point is colored red. On the other hand, the contacts approaching the Vander Waals interval value are colored white. Lastly, blue is used for longer contacts. The d_{norm} surface is illustrated using the red-blue-white color scheme in **Fig. 6**, in addition to shape index and curvedness maps. The three-dimensional HS derived from the title compound structure is represented in **Fig. 7**, where d_{norm} is mapped over the range of –0.398 (blue) to 1.569 (red), with a total volume of 525.81 $Å^3$ and a surface area of 472.64 $Å^2$. The distribution of these surfaces reveals the regions that are exposed to both strong and weak interactions. The two-dimensional fingerprint maps are shown in **Fig. 8**. These plots can be used to define the nature of the intermolecular contacts between the atoms inside and outside the molecule. They also provide the percentage contribution of each contact type to the total HS **[19]**. For the title molecule, the two-dimensional fingerprint plot indicates that H…H makes the most contacts, forming 23.6% of HS. The rest of the fingerprint map is made up of O…H/H…O (17.8%), F…H/H…F (14%), C…C (4.2%), O…C/C…O and N…H/H…N (both 3.6%), and S…C/C…S (2.8%) contact areas. Remarkably, the molecular structure is stabilized by π-π stacking intermolecular interactions, which are indicated by red and blue triangles on the shape index surface (**Fig. 6**). Due to the presence of aromatic ring carbon atoms inside the surface, the blue triangles have convex areas, whereas the red triangles have concave areas.

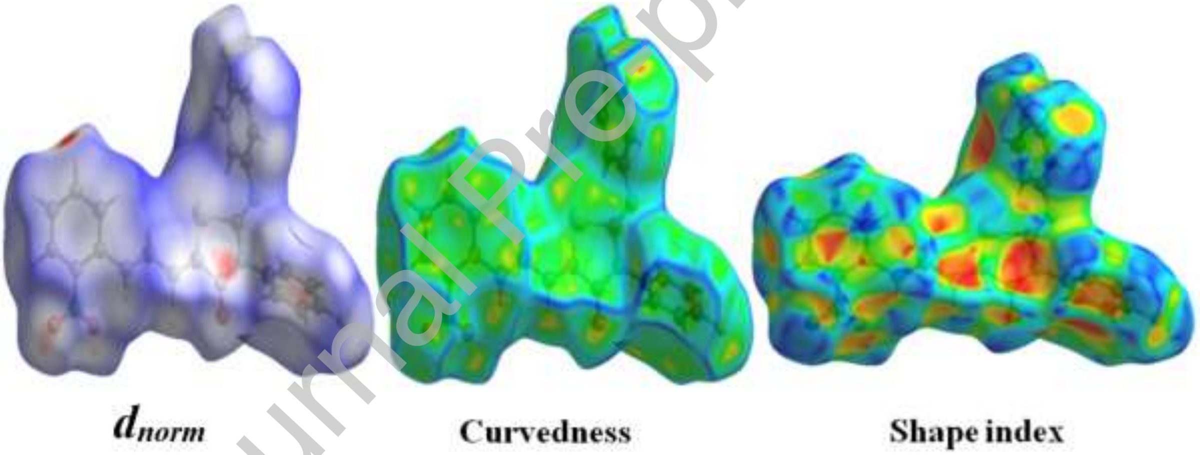

Fig. 6. d_{norm} HS, Curvedness and shape index maps for F2NTh.

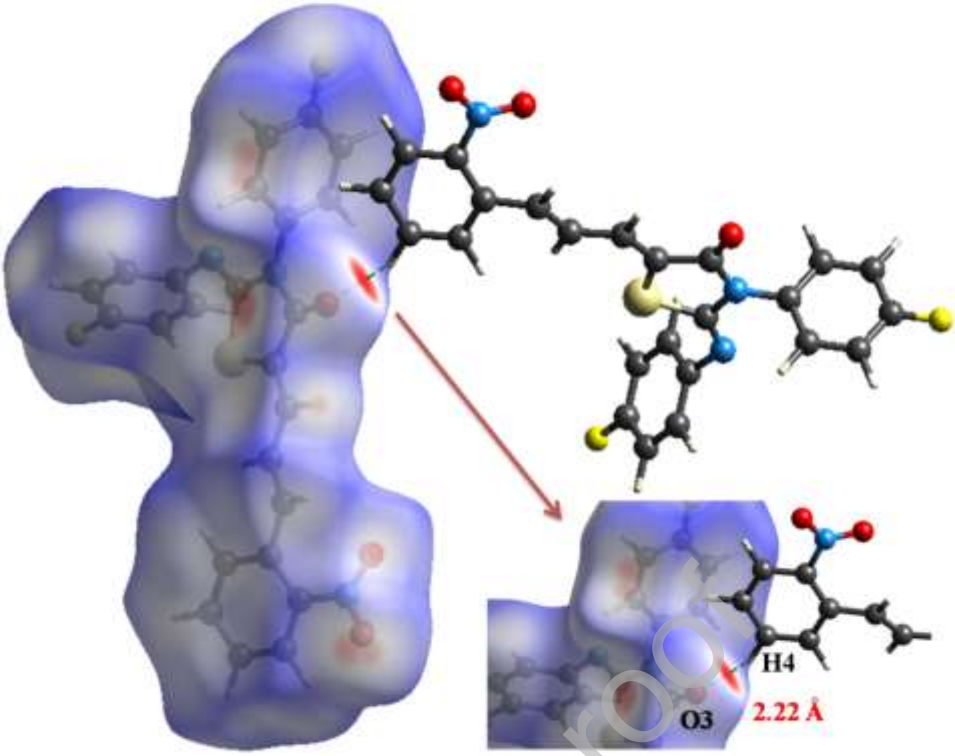

Fig. 7. Molecular HS map showing intermolecular interactions of F2NTh.

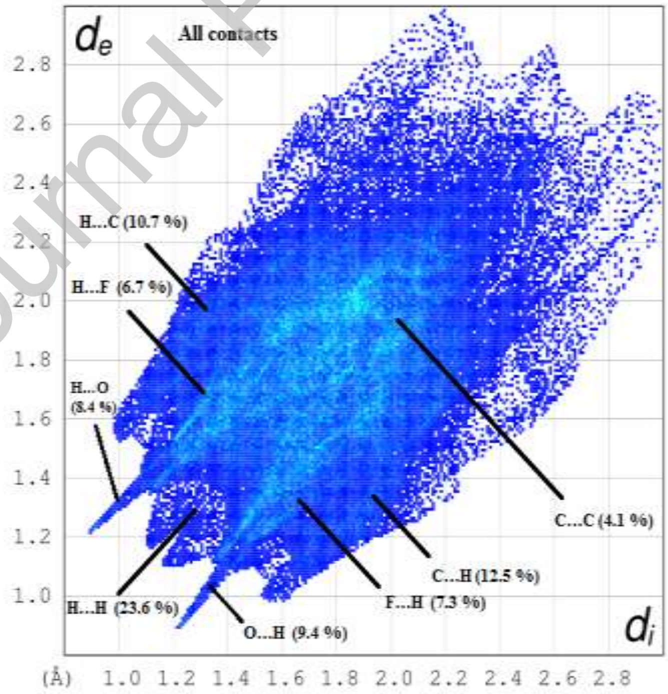

Fig. 8. 2D fingerprint plot for F2NTh revealing the contribution of each interaction to the total HS.

3.4.3. Reduced density gradient (RDG) analysis

The RDG methodology, based on electronic density, aims to reveal the nature of non-covalent interactions, including steric effects, H-bonds, and van der Waals interactions **[87]**. These weak interactions are fundamental for the comprehension of the exploration of many biological systems and represent an essential tool for understanding how molecules interact with each other **[88]**. By conducting the RDG study, we will be able to visualize the regions of strongest electronic interactions, which may be essential for understanding preferred interaction sites. In addition, the strength of these interactions can be quantified, helping us to assess their relative importance compared with other intermolecular forces. These previous interactions and their graphic representation are obtained from the following equation **[89]**:

$$RDG(r) = \frac{1|\nabla\rho(r)|}{2(3\pi r^2)^{\frac{1}{3}}\rho^{\frac{4}{3}}(r)}$$

where ρ(r) and ∇ρ(r) are the electron density and the gradient of ρ(r) at the point r, respectively. The different forms of interaction and their strengths were identified using the λ2 value. The graphical representation of ρ(r) versus sign (λ2) ρ informs us usefully about the strength and nature of interactions. The non-bonding interactions are denoted by the large positive values of sign (λ2)ρ. On the other hand, the presence of attractive interactions is denoted by the large negative sign of (λ2)ρ as the dipole-dipole or hydrogen bonding. The van der Walls interactions (weak interactions) appear when the value of (λ2)ρ is close to zero **[90]**. The 2D scatter plot was obtained by generating the graph of the RDG versus sign (λ2)ρ. The identification of various interactions occurring in F2NTh was achieved and represented in **Fig. 9**. Notably, a larger value than zero indicates bonding, while a value lower than zero indicates nonbonding **[91]**. As can be seen in the figure, the threshold value for the RDG scatter plots is set from -0.05 to 0.05, and the range of the RDG isosurface is from -0.035 to 0.02 a.u. It can also be observed in the figure that the red area indicates the strong repulsive interactions that are commonly observed in the barycenter of the aromatic rings, in our case the nitrophenyl, fluorophenyl, and thiazole rings. The brownish-green area indicates the presence of intermediary van der Walls interactions, weak interactions that are mostly due to H…H contacts; at last, strong attraction is marked by the blue area. The RDG scatter plots indicate that the blue region spans between 0.80 and 1.20 a.u., while the red and green regions span from −0.035 to +0.020 a.u. This observation can be explained by the fact that the strong hydrogen bonds are almost non-existent in F2NTh and can be confirmed by the established distances of the H-bonds using SC-XRD given in **Table 5**. Notably, the most significant hydrogen bonding is the C4–H4…O3 bond with a length of 2.22 Å. This can also be confirmed by referring to the 2D scatter plot, where we can see that the blue spots symbolizing the presence of strong H-bonds are almost non-existent too.

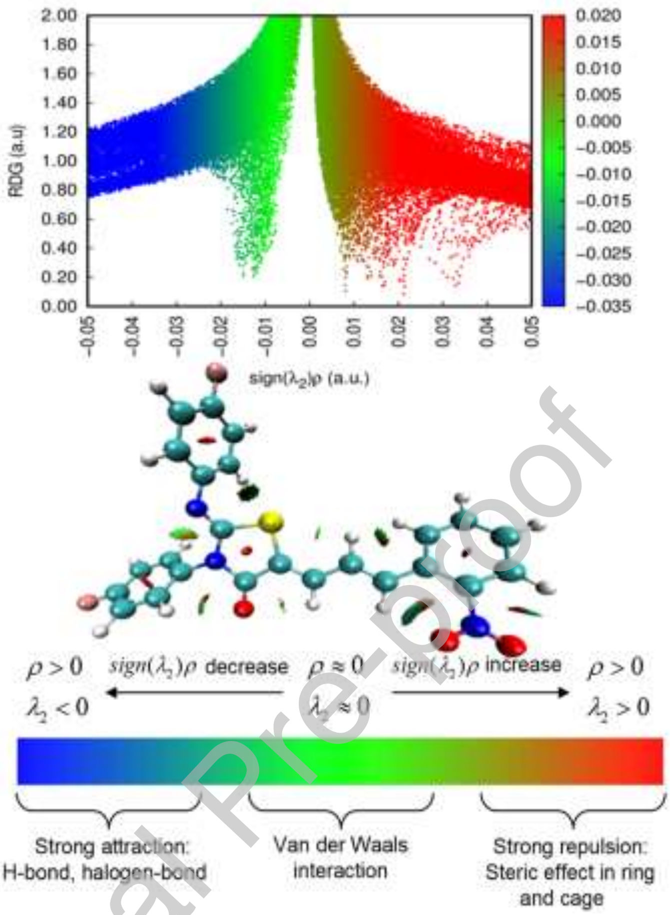

Fig. 9. Scatter density and 2D isosurface plots showing weak and strong interactions of F2NTh.

3.5. Frontier molecular orbitals and density of state analysis

Frontier molecular orbitals' (FMO's) are the highest occupied molecular orbital (HOMO) and lowest unoccupied molecular orbital (LUMO). These orbitals have the property of exchanging electrons; HOMO represents the ability to yield an electron, and LUMO represents the ability to receive an electron. They also have an essential contribution in the study of the optical properties of the molecule, as well as in quantum chemistry and the UV spectrum **[92]**. In addition, they inform us about the chemical stability and reactivity of organic molecules **[93]**. HOMO and LUMO energies may also allow us to characterize the reactivity and kinetic stability of molecules **[94]**. In addition, the charge transfer properties of the molecule are determined by the difference in energy between HOMO and LUMO **[95]**. The energy gap is a useful resource for the comprehension of the spectroscopic and chemical properties of organic molecules **[96]**. The amplitude of the energy separating HOMO and LUMO computed using the B3LYP functional with the 6-311G (d, p) basis set is 3.086 eV and 5.830 eV by the CAM-B3LYP functional. The value of the energy gap using the B3LYP level is relatively low in comparison with that obtained using the CAM-B3LYP level of theory and with other molecules **[59, 97]**, which indicates that the structure of the title compound is sufficiently stable and promotes its application as a non-linear optical material. Moreover, this relatively minor HOMO-LUMO energy gap explains the fact that a possible charge transfer interaction is occurring within the molecule **[98]**. It is common that molecules with a small boundary orbital gap are easily polarized, exhibit high chemical reactivity, and can be considered soft molecules **[99]**. Furthermore, various studies show that the HOMO, LUMO, and energy gap can be important quantum descriptors in determining the correlation in various chemical and biochemical systems **[100]**. The distribution of HOMO and LUMO orbitals with their corresponding energies is shown in **Fig. 10**. The first point that can be noticed from the represented figure is that the distribution of the two orbitals follows the conjugation plan in the title compound; the HOMO orbital is delocalized on both the thiazole ring and the fluorophenyl fragment (C13/C18). Whereas, the LUMO orbital is located on the nitrophenyl and allylidene fragments, which indicates that the charge transfer takes place from the fluorophenyl aromatic fragment to the nitrophenyl fragment. It can be explained by the fact that the NO_2 group is strongly attractive by the inductive and mesomeric effects and that the fluorine atom is a donor through its non-bonding doublets by the mesomeric effect. Other molecules with nearby structures have found a similar charge transfer result as the title compound using the same level of calculations **[91, 97]**. The density of states (DOS) is extensively used to describe the electronic behavior of molecular materials **[101]**. The FMO distribution was verified by partial DOS spectra performed using the B3LYP/6-311 G (d, p) basis set by the GaussSum program **[102]**. **Fig. 11** illustrates the DOS drawing, in which red and green lines indicate the occupied orbitals. The DOS diagram is usually the result of the combined effect of the donor and acceptor groups on the delocalization of electrons.

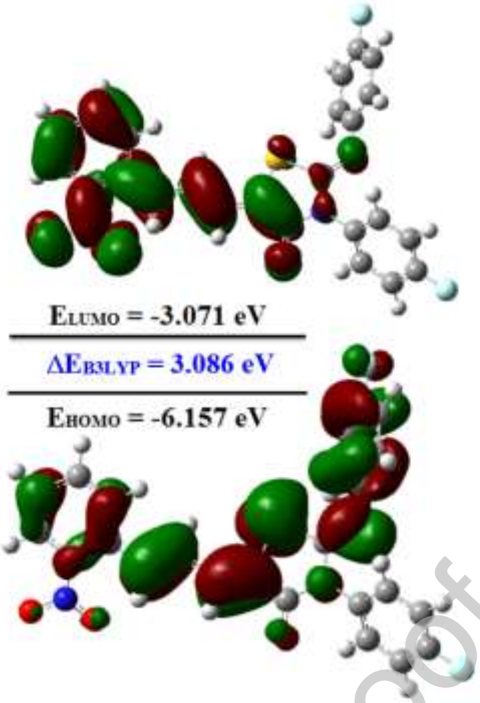

Fig. 10. HOMO and LUMO plot of F2NTh using the B3LYP functional.

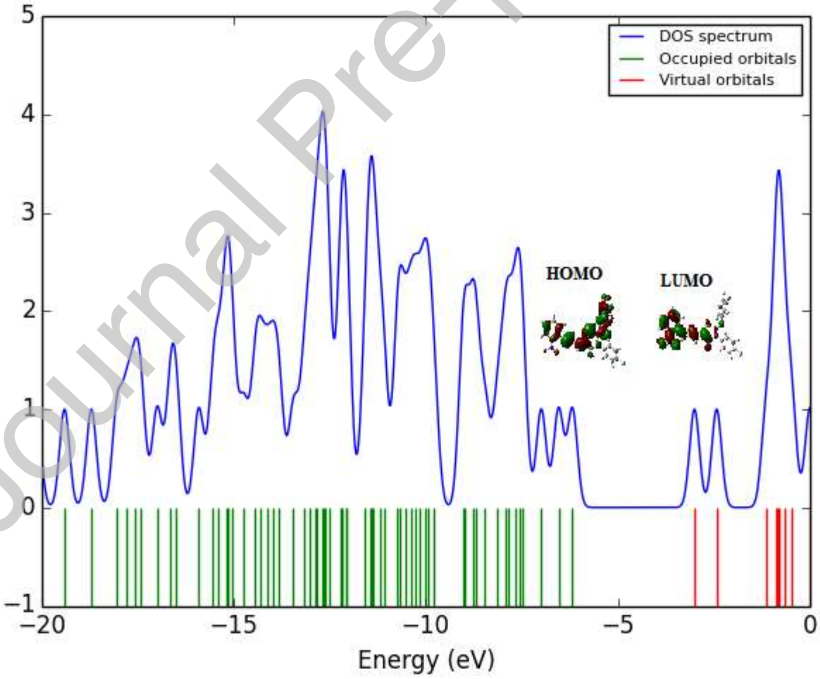

Fig. 11. Partial DOS diagram of F2NTh using the B3LYP functional.

3.6. **Global and local chemical reactivity descriptors**

3.6.1. Global chemical reactivity descriptors (GCRD)

The calculation of Global Chemical Reactivity Descriptors (GCRD) parameters highlights the correlation between chemical reactivity and molecular structure; they can also describe the stability of organic molecules **[74]**. GCRD parameters (ionization potential (I), electron affinity (A), electronegativity (χ), chemical potential *(P)*, chemical hardness (η), chemical softness (s), electrophilicity index (*ω*), and hyper-hardness (Γ)) were calculated through the use of HOMO and LUMO energy values and are listed in **Table 7** using the following equations **[103]**:

$$I = -E_{HOMO},\ A = -E_{LUMO},\ \chi = \frac{(I + A)}{2},\ P = -\frac{(I+A)}{2},\ \eta = \frac{(I-A)}{2},\ s = \frac{1}{2\eta},\ \omega = \frac{P^2}{2\eta}$$

$$\Gamma = E_{LUMO} - 2E_{HOMO} + E_{HOMO-1}$$

Where I = $-E_{HUMO}$ and A = $-E_{LUMO}$ are the ionization potential and electron affinity, respectively. The global electrophilicity index (*ω*) informs us about the electrophilic behavior of the molecule, with a reasonably high value of 7.88 eV for B3LYP and 4.17 eV for CAM-B3LYP. The low chemical hardness (η) of 1.54 eV for B3LYP and 2.92 eV for CAM-B3LYP may indicate that charge transfer is taking place within the molecule. The stability of the title molecule is confirmed by the negative value of the chemical potential, which is of the order of −4.61 eV for B3LYP and −4.65 eV for CAM-B3LYP. The chemical stability can also be confirmed by the positive value of the hyper-hardness parameter (Γ) **[19, 20]**, which is valued at +2.69 eV for B3LYP and +5.46 eV for CAM-B3LYP.

Table 7

Calculated quantum chemical molecular descriptors for F2NTh

Parameters (eV)	E_{HOMO}	E_{LUMO}	ΔE	I	A	χ	*P*	η	*s*	*ω*	Γ
B3LYP	−6.157	−3.071	3.086	6.16	3.07	4.61	−4.61	1.54	0.32	7.88	2.69
CAM-B3LYP	−7.564	−1.734	5.830	7.56	1.73	4.65	−4.65	2.92	0.17	4.17	5.46

3.6.2. Fukui functions (FF)

The most commonly used local reactivity parameters are the Fukui functions, which are typically employed to characterize the nucleophilic and electrophilic reactivity of chemical entities. They also describe a molecular system's electronic behavior and help in the investigation of molecular stereoselectivity **[104]**. Their definition is given as the derivative of the electron density versus the charge in the electron number density, keeping the positions of the nuclei unchanged **[105]**. The general Fukui function is expressed by **[106]**:

$$f(\vec{r}) = \left(\frac{\partial \rho(\vec{r})}{\partial N}\right) v(r)$$

where $\rho(\vec{r})$, N and $v(r)$ are the electronic density, number of electrons, and external potential extended by the nucleus, respectively. To study the tendency of each atom in the molecule, with a numerical value indicating the capacity of the atoms to be reactive sites, we used Fukui functions calculated according to the following equations **[107]**:

$$fk^{+} = qk\ (N+1) - q_k\ (N)$$

$$fk^{-} = qk\ (N) - q_k\ (N-1)$$

$$fk^{0} = \frac{qk\ (N+1) - qk\ (N-1)}{2}$$

Where fk^{+} represents nucleophilic attack, fk^{-} electrophilic attack, and fk^{0} is the free radical attack, in these equations; qk is the atomic charge at the k_{th} atomic site in the neutral (N), cationic (N+1) and anionic (N-1) chemical entities. From the natural bond orbital charges, it was able to calculate the values of the Fukui functions **[108]**. To investigate the local electrophilic indices, the global electrophilicity indices (ω) and Fukui indices (fk^{+}, fk^{-}) were linked together according to the following equations **[109]**:

$$\omega_k^{+} = \omega f_k^{+} \rightarrow \text{for nucleophilic attack}$$

$$\omega_k^{-} = \omega f_k^{-} \rightarrow \text{for electrophilic attack}$$

The results associated with the Fukui functions for the atoms of the title molecule are reported in **Table 8**. Atoms with a high value of softness ΔS_k are very susceptible to radical attacks **[110]**. In this context, we have calculated the values of this parameter in order to confirm the presence of atoms that can be exposed to this sort of interaction. According to **Table 9**, the low calculated local softness values indicate a poor possibility of susceptible sites to radical attacks and can be explained by the fact that our system is conjugated and influenced by the electronics effect (mesomeric) resulting from the conjugation of our system, which is more predominant than the electronegativity effect. Then, it can be presumed that the atoms are more susceptible to electrophilic and nucleophilic attacks, leading us thereafter to calculate more parameters to confirm this fact. These additional parameters, which are important to differentiate between electrophilic and nucleophilic attacks and predict the important reactive sites of the molecule **[111]**, are the dual (Δf_k) and multiphilic ($\Delta \omega_k$) descriptors. They have been calculated based on the following equations **[74]**:

$$\Delta f_k = [f_k^{+}{}_{(r)} - f_k^{+}{}_{(r)}]$$

$$\Delta \omega_k = \omega\ (f_k^{+} - f_k^{+}) = \omega\ \Delta f_k$$

Where the positive values of (Δf) and ($\Delta \omega$) confirm the elctrophilic character of the reactive molecular sites and promote nucleohilic attacks. The negative values of these last parameters show the nucleophilic character of the reactive molecular sites and favor electophilic attacks. Based on this statement, we deduced from the calculated results of **Table 8** that the nucleophilic sites are O1, O2, O3, N1, C1, C2, C3, C4, C5, C6, C8, C10, C11, C19, and C20 atoms, while the electrophilic sites are the S1, F1, F2, N2, N3, C7, C9, C12, C13, C14, C15, C16, C17, C18, C21, C22, C23, and C24 atoms.

Table 8

Local reactivity descriptors calculated by B3LYP/6-311G (d, p for F2NTh.

Atoms	Fukui functions (eV)				Local electrophilicity index (eV)			Local softness (eV)		
	f_k^-	f_k^+	f_k^0	Δf_k	ω_k^-	ω_k^+	$\Delta\omega_k$	S_k^-	S_k^+	ΔS_k
S1	0.0506	0.1186	0.0846	0.0680	0.3988	0.9347	0.5358	0.0164	0.0385	0.0220
F1	0.0145	0.0419	0.0282	0.0274	0.1144	0.3305	0.2161	0.0047	0.0136	0.0089
F2	0.0153	0.0188	0.0170	0.0034	0.1208	0.1480	0.0272	0.0049	0.0061	0.0011
O1	0.0585	0.0051	0.0318	-0.0534	0.4613	0.0402	-0.4210	0.0190	0.0016	-0.0173
O2	0.0815	0.0324	0.0570	-0.0491	0.6424	0.2555	-0.3869	0.0264	0.0105	-0.0159
O3	0.0564	0.0386	0.0475	-0.0178	0.4444	0.3041	-0.1403	0.0183	0.0125	-0.0057
N1	0.0199	0.0023	0.0111	-0.0176	0.1573	0.0181	-0.1392	0.0064	0.0007	-0.0057
N2	-0.0065	0.0092	0.0013	0.0157	-0.0512	0.0727	0.1239	-0.0021	0.0029	0.0051
N3	0.0393	0.0605	0.0499	0.0211	0.3096	0.4765	0.1668	0.0127	0.0196	0.0068
C1	0.0200	0.0181	0.0190	-0.0019	0.1581	0.1425	-0.0155	0.0065	0.0058	-0.0006
C2	0.0541	0.0401	0.0471	-0.0140	0.4265	0.3158	-0.1106	0.0175	0.0130	-0.0045
C3	0.0795	0.0568	0.0681	-0.0227	0.6266	0.4474	-0.1791	0.0258	0.0184	-0.0073
C4	0.0716	0.0300	0.0508	-0.0415	0.5642	0.2369	-0.3273	0.0232	0.0097	-0.0134
C5	0.0404	0.0230	0.0317	-0.0173	0.3184	0.1819	-0.1365	0.0131	0.0074	-0.0056
C6	0.0248	-0.0134	0.0056	-0.0383	0.1956	-0.1062	-0.3018	0.0080	-0.0043	-0.0124
C7	0.0557	0.0824	0.0690	0.0267	0.4388	0.6495	0.2107	0.0180	0.0267	0.0086
C8	0.0590	0.0207	0.0399	-0.0382	0.4650	0.1636	-0.3013	0.0191	0.0067	-0.0124
C9	0.0566	0.0749	0.0658	0.0183	0.4462	0.5906	0.1444	0.0183	0.0243	0.0059
C10	0.0352	0.0063	0.0208	-0.0289	0.2779	0.0501	-0.2278	0.0114	0.0020	-0.0093
C11	0.0382	0.0128	0.0255	-0.0254	0.3012	0.1011	-0.2000	0.0124	0.0041	-0.0082
C12	0.0109	0.0125	0.0117	0.0015	0.0863	0.0986	0.0122	0.0035	0.0040	0.0005
C13	-0.0169	-0.0046	-0.0108	0.0123	-0.1337	-0.0364	0.0973	-0.0055	-0.0015	0.0040
C14	0.0010	0.0412	0.0211	0.0402	0.0078	0.3252	0.3173	0.0003	0.0134	0.0130
C15	0.0215	0.0552	0.0384	0.0337	0.1697	0.4353	0.2656	0.0069	0.0179	0.01094
C16	0.0092	0.0304	0.0198	0.0212	0.0726	0.2398	0.1672	0.0029	0.0098	0.0068
C17	0.0264	0.0615	0.0440	0.0350	0.2086	0.4843	0.2757	0.0086	0.0199	0.0113
C18	0.0206	0.0612	0.0409	0.0405	0.1625	0.4821	0.3196	0.0067	0.0198	0.0131
C19	-0.0057	-0.0193	-0.0125	-0.0135	-0.0455	-0.1521	-0.1065	-0.0018	-0.0062	-0.0043
C20	0.0046	-0.0009	0.0018	-0.0056	0.0369	-0.0078	-0.0448	0.0015	-0.0003	-0.0018
C21	0.0272	0.0306	0.0289	0.0033	0.2147	0.2410	0.0262	0.0088	0.0099	0.0010
C22	0.0088	0.0099	0.0093	0.0011	0.0693	0.0782	0.0089	0.0028	0.0032	0.0003
C23	0.0261	0.0322	0.0292	0.0061	0.2061	0.2541	0.04804	0.0084	0.0104	0.0019
C24	0.0003	0.0100	0.0052	0.0096	0.0029	0.0789	0.0759	0.0001	0.0032	0.0031

3.7. **Molecular electrostatic potential (MEP) analysis**

The MEP is well identified as the interaction between the molecular charge distribution (electrons and nuclei) and the positive unit charge at any point in space surrounding the molecule. The electrostatic potential experimentally determined using X-ray diffraction as well as by calculation remains one of the most commonly used techniques for predicting the reactivity of molecules **[112]**. Mathematically, MEP can be defined by the following equation:

$$\mathrm{V}(\vec{\mathrm{r}}) = \sum_{\mathrm{A}} \frac{\mathrm{Z_A}}{\left|\vec{\mathrm{R}}_{\mathrm{A}} - \vec{\mathrm{r}}\right|} - \int \frac{\rho(\vec{\mathrm{r}'})}{\left|\vec{\mathrm{r}'} - \vec{\mathrm{r}}\right|}\, d\vec{\mathrm{r}'}$$

Where Z_A is the nucleus charge, which is located at R_A, and $\rho(r')$ is the electron density. To describe the reactive sites for electrophilic and nucleophilic attacks of the investigated molecule, the MEP map for F2NTh is illustrated in **Fig. 12**. The range of the limits for total electron density is over -5.342×10^{-2} to $+5.342\times10^{-2}$ a.u. As can be seen in **Fig. 12**, the possible sites for electrophilic attacks are the oxygen atoms O1, O2, and O3. The blue regions (positive areas) are located on the hydrogen atoms of the phenyl rings, indicating a possible site for nucleophilic attacks. It can also be seen that the yellow color covers the two fluorine atoms F1 and F2, indicating a relatively negative potential that can be explained by the H-bonds formed with the fluorine atoms. The neighboring regions close to the sulfur atom are positive due to the surrounding electropositive atoms **[66]**. These sites can give us information about susceptible regions to intermolecular interactions and evidence of biological activity **[113]**.

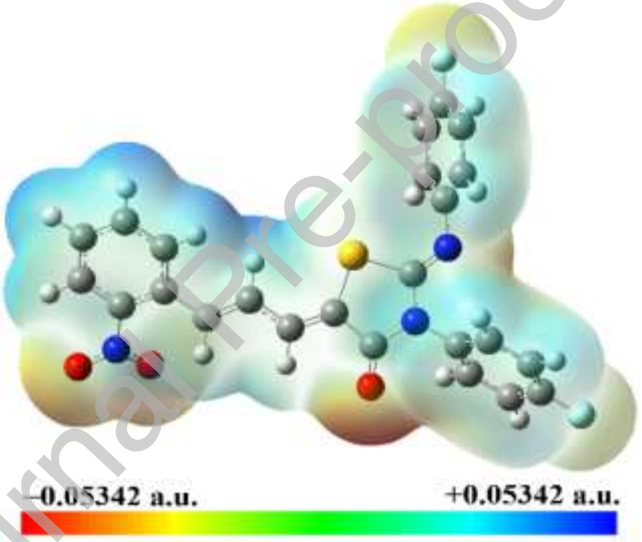

Fig. 12. MEP map calculated using B3LYP.

3.8. Population atomic charge analysis (MPA, NPA, MC5, ESP)

The distribution of electron density within a molecule is identified via population atomic charge analysis. This research provides important additional knowledge on the molecule's chemical composition and electrical structure. Furthermore, it is possible to determine areas of high and low electron density by calculating atomic charges, which can explain the molecule's reactivity and binding behaviors. Population atomic charge analysis is also essential for understanding intermolecular interactions and anticipating the activity of compounds in various environments. This analysis provides valuable insights into the electronic structure and chemical properties of the molecule **[114]**. The calculation of atomic charges is crucial in the application of quantum chemical calculations in molecular systems. Atomic charges can affect dipole moment, electronic structure, molecular polarizability, NLO properties, and acid-base behavior **[115]**. They can also play an important role in describing electron distribution in organic molecules. Among the oldest methods of calculating charges, Mulliken's method **[116]** remains the fastest and least expensive at the same time, but due to the lack of deficiencies it represents, such as the dependence on the basis set **[117]**, other methods have been introduced, such as NPA (natural population analysis), MC5 (Hirshfeld charges), and ESP (Merz-Kollman charges). Natural population analysis (NPA) is known to be a more reliable approach as it considers the impact of electron density and the polarization effect **[118]**. The Hirshfeld approach has the advantage of being able to eliminate randomness in the choice of promolecule and enhance the magnitude of the charges. Therefore, the resulting Hirshfeld charges correlate well with the atomic charges obtained from the electrostatic potential **[119]**. Merz Kollman charges provide the best potential and moments; their disadvantage is a low dependence on the way the molecule is oriented **[120]**. Based on these atomic charge descriptions, we performed the charge analysis using the B3LYP/6-311G (d, p) level for comparative purposes, with the aim also of confirming the electrostatic potential (electrophilic ornucleophilic sites) of the title molecule studied in previous sections. Thereafter, for a better comparison, the obtained results have been reported in **Table 9** and plotted in **Fig. 13**. As anticipated, most negative charges were located on the O, N, and F (except N1 of the nitro group) atoms for all four calculated types of atomic charges. Otherwise, the electrophilic regions were located on the C6, C8, C10, C15, C17, C21, and C23 atoms. The remaining carbons of the title molecule and S1 and N1 hold positive charges. Furthermore, the atomic charges support the presence of hydrogen bonds (C–H…O) and (C–H…F) which is the case for the most important hydrogen bonds determined in the experimental section (hydrogen bonding) that occur with the oxygen and fluorine atoms (C21–H21…O2, C21–H21…O3, C24–H24…F1 and C17–H17…F2). Atomic charges also confirmed π-π stacking interactions occurring in the aromatic rings. The electrophilic and nucleophilic regions of the MEP surface show similar results to the charge analysis especially by MPA and NPA, which were subsequently verified by the Fukui indices. According to **Fig. 13**, we noticed that the MPA, NPA and ESP models gave similar results as well as a close distribution of atomic charges, except for the MC5 charges model, which represents a quite different plot. These differences between the three MPA, NPA, and ESP charge models and the MC5 model are due to different approaches in the estimation of the atomic charges **[121]**. It can be deduced from this study that the title molecule is considered to have a significant electrophilic character previously determined with a high value of the electophilicity index (*ω)* of 7.875 eV.

Table 9

Calculated atomic charges by MPA, NPA, ESP and MC5 models for F2NTh

Atoms	MPA	NPA	MC5	ESP
S1	0.233	0.277	−0.029	−0.151
F1	−0.235	−0.350	−0.108	−0.214
F2	−0.228	−0.345	−0.101	−0.211
O1	−0.264	−0.380	−0.194	−0.398
O2	−0.256	−0.378	−0.201	−0.412
O3	−0.320	−0.570	−0.266	−0.475
N1	0.145	0.513	0.263	0.695
N2	−0.495	−0.493	−0.018	−0.223
N3	−0.326	−0.504	−0.157	−0.517
C1	0.112	0.084	0.026	0.011
C2	0.103	−0.176	0.023	−0.206
C3	0.021	−0.187	0.027	−0.080
C4	0.045	−0.166	0.033	−0.118
C5	0.034	−0.173	0.022	−0.157
C6	−0.011	−0.055	0.008	0.123
C7	0.106	−0.137	0.021	−0.292
C8	−0.004	−0.202	0.015	−0.090
C9	0.154	−0.169	0.040	−0.025
C10	−0.414	−0.246	−0.032	−0.190
C11	0.526	0.676	0.179	0.567
C12	0.222	0.371	0.117	0.391
C13	−0.012	0.123	0.037	0.363
C14	0.062	−0.213	0.001	−0.150
C15	−0.013	−0.260	0.002	−0.316
C16	0.240	0.417	0.086	0.381
C17	−0.015	−0.259	0.003	−0.290
C18	0.065	−0.192	0.003	−0.229
C19	0.086	0.136	0.038	0.206
C20	0.117	−0.165	0.017	−0.199
C21	−0.021	−0.263	0.008	−0.266
C22	0.252	0.437	0.097	0.389
C23	−0.018	−0.262	0.010	−0.275
C24	0.107	−0.165	0.023	−0.170

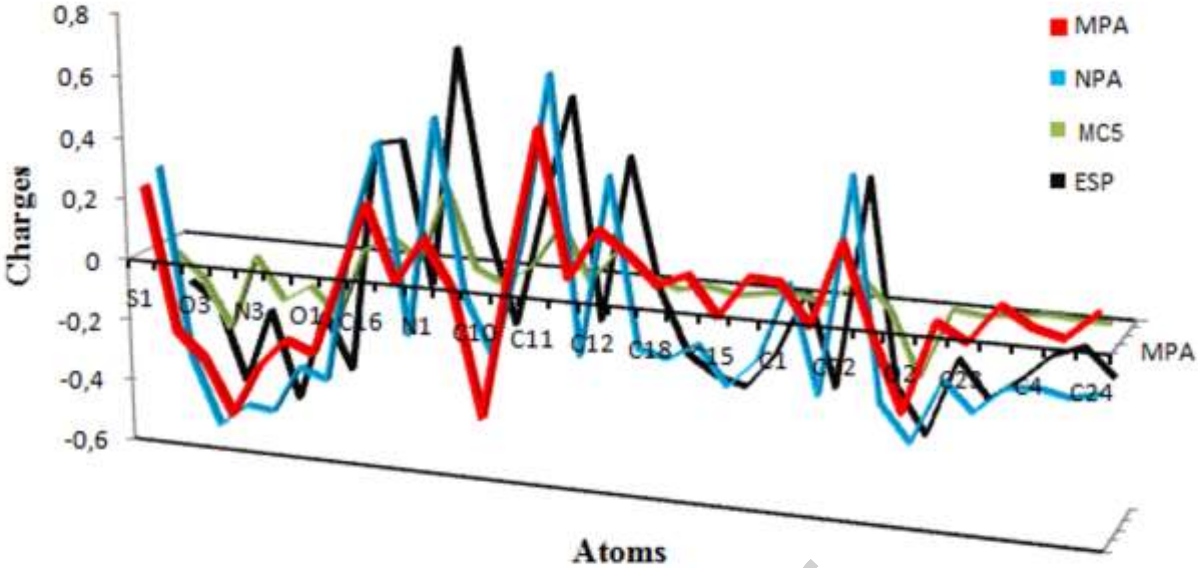

Fig. 13. The 3D-graphic representation of the attribution of MPA, NPA, MC5 and ESP charges to F2NTh atoms

3.9. **Thermodynamic parameters**

The theoretical calculation of the thermodynamic properties of the title compound at 298.15 K was established from the predicted harmonic frequencies. Among the parameters that have been calculated are zero-point vibrational energy, rotational constants, rotational temperatures, thermal energy, molecular capacity at constant volume, entropy, zero-point correction, thermal correction to energy, thermal correction to enthalpy, and thermal correction to Gibbs free energy. The theoretical calculated values using B3LYP and CAM-B3LYP functionals with a 6-311G (d, p) basis set are listed in **Table 10**. We noticed in the results that values obtained from the two levels of theory are approached, except for the molecular capacity at constant volume, where we found a value of 105.120 cal.mol^{-1}.K^{-1} for the B3LYP and 86.025 cal.mol^{-1}.K^{-1} for the CAM-B3LYP. An apparent difference was also noticed in the entropy values, which are about 186.170 Cal.mol^{-1}.K^{-1} and 157.273 Cal.mol^{-1}.K^{-1} for the B3LYP and CAM-B3LYP, respectively. Thermodynamic functions such as entropy (S), constant heat capacity (Cp), and enthalpy variation ($\Delta H = H_T - H_0$) for a temperature range between 100 and 1000 K were calculated and reported in **Table 11**. The collected data indicate a consistent increase in heat capacities, entropies, and enthalpies as the temperature rises. **Table 11** further illustrates that the calculated results using both B3LYP and CAM-B3LYP exhibit a similar evolution. Notably, the values obtained from the B3LYP consistently surpass those obtained from the CAM-B3LYP. The above results are of great interest for predicting the directions of chemical reactions according to the second law of thermodynamics **[65, 122]**. **Fig. 14** shows the evolution of the thermodynamic parameters calculated with temperature. It should be noted that the same plots were obtained for B3LYP and CAM-B3LYP functionals.

Table 10

Thermodynamic parameters of F2NTh calculated at 298.15 K in the ground state.

Thermodynamic parameters	6-311G (d, p)	
	B3LYP	CAM-B3LYP
Zero-point vibrational energy (Kcal.mol^{-1})	214.344	213.505
Rotational constant (GHZ)	0.138 0.052 0.039	0.140 0.056 0.041
Rotational temperature (Kelvin)	0.006 0.002 0.001	0.006 0.002 0.001
Energy (Kcal.mol^{-1})		
Total	231.389	227.372
Translational	0.889	0.889
Rotational	0.889	0.889
Vibrational	229.611	225.594
Molecular capacity at constant volume (Cal .mol^{-1}.K^{-1})		
Total	105.120	86.025
Translational	2.981	2.981
Rotational	2.981	2.981
Vibrational	99.158	80.063
Entropy (Cal.mol^{-1}.K^{-1})		
Total	186.170	157.273
Translational	44.287	44.287
Rotational	38.245	38.128
Vibrational	103.638	74.858
Zero point correction (Hartree/Particle)	0.341	0.340
Thermal correction to Energy	0.368	0.362
Thermal correction to Enthalpy	0.369	0.363
Thermal correction to Gibbs Free Energy	0.281	0.288

Table 11

Calculated thermodynamic parameters for F2NTh at different temperatures

T (K)	B3LYP/6-311G (d, p)			CAM-B3LYP/6-311G (d, p)		
	Cp (J/molK)	S (J/molK)	ΔH (KJ/mol)	Cp (J/molK)	S (J/molK)	ΔH (KJ/mol)
100	335.70	613.97	19.68	188.806	496.43	12.40
200	595.87	924.69	66.00	316.74	665.47	37.52
298.15	**862.61**	**1212.23**	**134.74**	**449.15**	**816.56**	**75.09**
300	867.90	1218.01	139.26	451.77	819.57	75.99
400	1114.14	1502.36	238.69	574.07	966.76	127.44
500	1316.56	1773.56	360.61	674.70	1106.08	190.07
600	1476.77	2028.34	500.59	754.45	1236.43	261.68
700	1603.37	2265.87	654.84	817.55	1357.66	340.40
800	1704.73	2486.83	820.43	868.13	1470.25	424.78
900	1787.19	2692.54	995.16	909.31	1574.96	513.72
1000	1855.22	2884.47	1177.39	943.32	1672.58	606.40

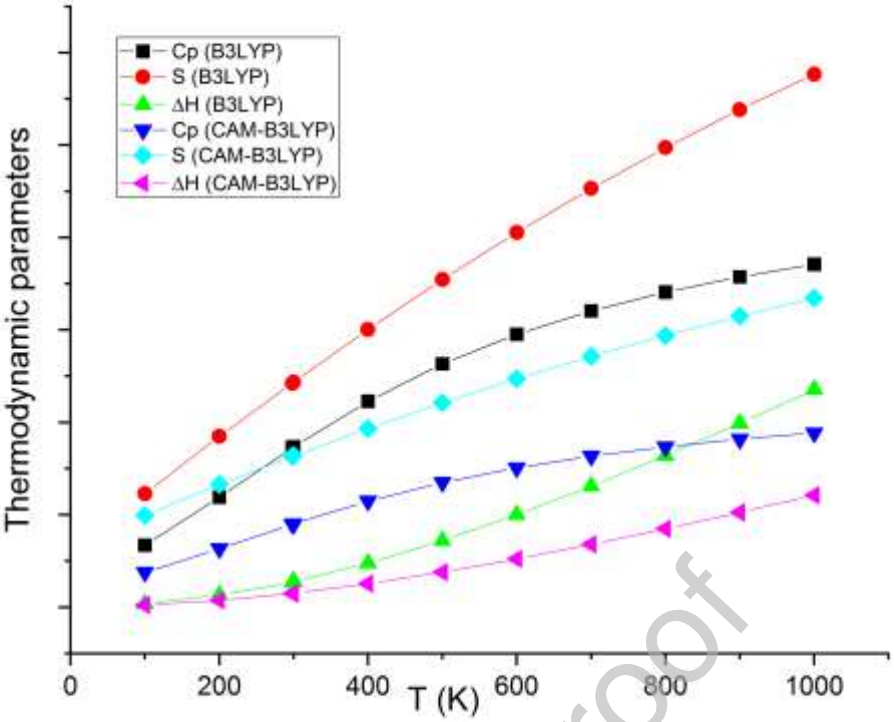

Fig. 14. The evolution curve of thermodynamic properties of F2NTh versus the temperature using B3LYP and CAM-B3LYP functionals.

3.10. NLO analysis

Fluoro-substituted organic molecules containing one or more fluorine atoms in their structure are a very important class of materials. These substitutions can significantly alter the properties and reactivity of the organic compound. Fluorine's high electronegativity leads to considerable electronic polarization within the molecule under study. More specifically, the presence of two fluorine atoms results in a significant dipole moment, giving rise to an unequal distribution of electrical charges **[123, 124]**. This polarity can also influence the polarizability and hyperpolarizability parameters, making the molecule more sensitive to electric field changes.

Theoretical calculation methods have proven useful for the prediction of polarization and hyperpolarization, avoiding the costly experimental synthesis work necessary for the measurement of optic nonlinear (NLO) properties. The estimation of the total dipole moment (μ), the mean polarizability (α), and the first and second hyperpolarizabilities (β and γ) allows a better understanding of the relationship between molecular structure and NLO properties **[125]**. Recently, organic molecules with conjugated π-electrons have received considerable attention because of their eventual applications as non-linear optical materials **[82]**. The NLO phenomenon can be defined as an interaction between the electromagnetic field and the material that will subsequently create new fields differing in their diffusion properties. A molecule with high dipole moment, polarizability, and hyperpolarizability values is more active in NLO. The Taylor series expansion has been used to calculate the total energy (E) of the material in the presence of an intensive electric field **[126]**. The following equation provides the total energy:

$$E(F) = E(0) - \mu_i F_i - \frac{1}{2!}\alpha_{ij} F_i F_j - \frac{1}{3!}\beta_{ijk} F_i F_j F_k - \frac{1}{4!}\gamma_{ijkl} F_i F_j F_k F_l \ldots$$

where the indices (*i*,*j*,*k*) denote the various components of the cartesian coordinate system (*x*,*y*,*z*). *E*(0) represents the energy of the compound in the absence of an external electric field *F*. μ_i is the electric dipole moment, and F_i indicates the i^{th} cartesian component of the applied electric field. α, β and γ are the linear mean polarizability, and first- and second-order hyperpolarizabilities, respectively. The molecular dipole moment (μ), mean polarizability ($\langle\alpha\rangle$), the anisotropy of the polarizability $\Delta\alpha$, and first- and second-order hyperpolarizabilities (β and γ) were calculated using the following equations:

$$\mu = \left(\mu_x^2 + \mu_y^2 + \mu_z^2\right)^{1/2}$$

$$\langle\alpha\rangle = {}^{1}/_{3}\left(\alpha_{xx} + \alpha_{yy} + \alpha_{zz}\right)$$

$$\Delta\alpha = 2^{-1/2}\left(\left(\alpha_{xx} - \alpha_{yy}\right)^2 + \left(\alpha_{yy} - \alpha_{zz}\right)^2 + \left(\alpha_{zz} - \alpha_{xx}\right)^2 + 6\alpha_{xx}^2\right)^{1/2}$$

$$\beta_{tot} = \left(\beta_x^2 + \beta_y^2 + \beta_z^2\right)^{1/2}$$

where

$$\beta_x = (\beta_{xxx} + \beta_{xyy} + \beta_{xzz});\ \beta_y = (\beta_{yyy} + \beta_{yxx} + \beta_{yzz});\ \beta_z = (\beta_{zzz} + \beta_{zxx} + \beta_{zyy})$$

$$< \gamma >= \frac{1}{5}\left[\gamma_{xxxx} + \gamma_{yyyy} + \gamma_{zzzz} + 2\left(\gamma_{xxyy} + \gamma_{xxzz} + \gamma_{yyzz}\right)\right]$$

The values of polarizability (α), and first and second hyperpolarizabilities (β_{tot}, γ) are reported in atomic units (a.u.), so the calculated values have been converted to electrostatic units (esu) (α : 1 a.u = 0.148×10^{-24} esu, β : 1 a.u = 8.639×10^{-33} esu, and for γ: 1 a.u = 5.037×10^{-40} esu).

3.10.1. Static NLO properties

The values of NLO parameters were predicted using B3LYP and CAM-B3LYP functionals with the 6-311G (d, p) basis set, and the results are assembled in **Table 12**. The dipole moment of a molecule is an essential feature describing the movement of charge through molecules **[127]**. The calculated dipole moment *(μ)* values are 4.93 and 5.09 Debye obtained with B3LYP and CAM-B3LYP functionals, respectively. The direction of the dipole moment vector differs depending on the positive and negative charge centers. For the title molecule, this direction is shown in **Fig. 15**. As can be seen, the vector is directed from the fluoro-phenyl (ring 2) to the nitro-phenyl (ring 1), which confirms the charge transfer discussed above. As can be seen from **Table 12**, the final predicted values of $\langle \alpha \rangle$ are 56.232 and 53.143 $\times 10^{-24}$ esu by B3LYP and CAM-B3LYP, respectively. For β_{tot}, the two functionals give predicted values of 28.0 and 13.4 $\times 10^{-30}$ esu. From the above results, we noticed that the theoretical calculated (β_{tot}) values for F2NTh using the two levels of theory are much greater than those of urea, which is considered a prototype molecule used in the study of the NLO properties of molecular systems **[128]**. Moreover, to assess the higher-order nonlinearity of the investigated molecule, the static second hyperpolarizability (γ) values are computed. The two values, 244.98 and 137.47 $\times 10^{-36}$ esu obtained by B3LYP and CAM-B3LYP, respectively, are rather different. However, that obtained with B3LYP functional is quite large. Therefore, the above results serve as validation of the title compound's strong NLO behavior.

Table 12

Calculated static NLO parameters for F2NTh (μ, Debye; $\langle\alpha\rangle$ and $\Delta\alpha$, $\times 10^{-24}$ esu; β_{tot}, $\times 10^{-30}$ esu; γ, $\times 10^{-36}$ esu).

Dipole moment	B3LYP	CAM-B3LYP
μ_x	0.653	0.810
μ_y	1.675	1.675
μ_z	–0.728	–0.744
μ (D)	**4.93**	**5.09**
α (0, 0)	B3LYP	CAM-B3LYP
α_{xx}	79.625	71.200
α_{yx}	11.468	11.964
α_{yy}	32.374	32.725
α_{zx}	11.695	11.639
α_{zy}	–4.287	–3.427
α_{zz}	56.697	55.502
⟨α⟩	**56.232**	**53.143**
Δα	**50.35**	**44.65**
$\beta_{\|\|}(0,0,0)$	B3LYP	CAM-B3LYP
β_{xxx}	35.600	15.893
β_{yxx}	16.030	9.836
β_{yxy}	7.246	5.286
β_{yyy}	2.848	2.194
β_{xxz}	–0.218	–0.951
β_{yxz}	–0.387	0.257
β_{yyz}	0.353	0.993
β_{zxz}	0.236	–1.496
β_{zyz}	–0.968	–1.481
β_{zzz}	0.744	0.022
β_{tot}	**28.00**	**13.40**

$\gamma_{\|\|}(0,0,0,0)$	B3LYP	CAM-B3LYP
γ_{xxxx}	669.751	297.726
γ_{yyyy}	23.358	15.831
γ_{zzzz}	78.812	69.876
γ_{xxyy}	69.750	37.333
γ_{xxzz}	142.427	103.757
γ_{yyzz}	14.282	10.852
γ	**244.98**	**137.47**

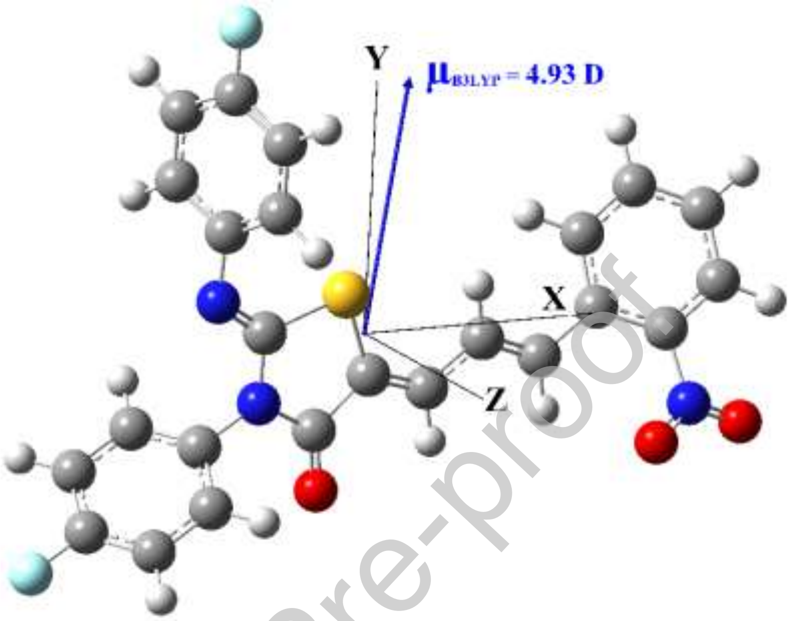

Fig. 15. The dipole moment direction of the title compound.

3.10.2. Dynamic NLO properties

Nowadays, for photonic devices, compounds with greater frequency-dependent NLO responses are of huge interest. In this section, we performed frequency-dependent calculations for our compound to further describe its NLO activity using the two functionals B3LYP and CAM-B3LYP. The corresponding findings are gathered in **Table 13**. As is well known, the frequency-dependent hyperpolarizabilities include the prediction of the electro-optic Pockels effect (PE), which corresponds to α $(-\omega, \omega)$ and $\beta_{||}(-\omega,\omega,0)$, and the second harmonic generation phenomenon (SHG), which corresponds to $\beta_{||}(-2\omega,\omega,0)$ at $\omega = 911.3$ nm. Likewise, the dc-Kerr effect (quadratic electro-optical Kerr effect) and dc-SHG are associated with $\gamma_{||}(-\omega;\omega,0,0)$ and $\gamma_{||}(2\omega;\ \omega,\ \omega,\ 0)$. Using both B3LYP and CAM-B3LYP functionals, α $(-\omega, \omega)$ values are 59.928 and 55.687 $\times 10^{-24}$ esu, respectively. As can be seen in **Table 13**, the components of the dynamic polarizability tensor have almost similar values, which makes it possible to have a value by B3LYP closer to that by CAM-B3LYP. The third-order NLO response, expressed by the second-order hyperpolarizability, is also predicted at 911.3 nm, which includes the electro-optic dc-Kerr effect (EOKE) and the electric field-induced second harmonic generation (EFISHG). The most important value of $\gamma_{||}(2\omega;\omega,\omega,0)$ (56281.5×10^{-36} esu) is obtained by B3LYP functional.

Table 13

Calculated dynamic NLO parameters for F2NTh ($\langle\alpha\rangle$ and $\Delta\alpha$, $\times10^{-24}$ esu; β_{tot}, $\times10^{-30}$ esu; γ, $\times10^{-36}$ esu), (ω = 911.3 nm).

Parameters	B3LYP		CAM-B3LYP	
Polarizability	$\alpha(-\omega,\omega)$		$\alpha(-\omega,\omega)$	
α_{xx}	87.514		76.027	
α_{yx}	13.594		13.447	
α_{yy}	33.464		33.646	
α_{zx}	13.891		13.347	
α_{zy}	–3.996		-3.114	
α_{zz}	58.807		57.387	
$\langle\alpha\rangle$	**59.928**		**55.687**	
$\Delta\alpha$	**58.09**		**49.59**	
First-order hyperpolarizability	$\beta_{\|\|}(-\omega,\omega,0)$	$\beta_{\|\|}(-2\omega,\omega,0)$	$\beta_{\|\|}(-\omega,\omega,0)$	$\beta_{\|\|}(-2\omega,\omega,0)$
β_{xxx}	65.236	1197.74	23.42	68.05
β_{yxx}	26.334	390.267	13.15	29.81
β_{yxy}	11.692	147.734	7.04	14.97
β_{yyy}	4.703	64.071	2.98	6.96
β_{xxz}	0.433	74.199	–1.20	1.98
β_{yxz}	–0.534	19.563	0.26	1.48
β_{yyz}	0.182	32.047	1.07	4.34
β_{zxz}	0.779	39.274	–1.84	–3.17
β_{zyz}	–0.833	11.514	–1.63	–2.22
β_{zzz}	0.538	7.1526	–0.36	–1.65
β_{tot}	**50.05**	**885.22**	**19.32**	**54.26**
Second-order hyperpolarizability	$\gamma_{\|\|}(-\omega;\omega,0,0)$	$\gamma_{\|\|}(2\omega;\omega,\omega,0)$	$\gamma_{\|\|}(-\omega;\omega,0,0)$	$\gamma_{\|\|}(2\omega;\omega,\omega,0)$
γ_{xxxx}	1353.33	212026.0	445.13	1425.08
γ_{yyyy}	41.167	4136.99	21.03	51.94
γ_{zzzz}	101.987	496.62	86.37	158.38
γ_{xxyy}	152.193	26065.3	57.15	180.62
γ_{xxzz}	230.181	2922.77	145.95	292.96
γ_{yyzz}	22.242	–54.174	13.01	23.77
γ	**452.30**	**56281.5**	**194.121**	**541.935**

4. Conclusions

In summary, new fluorine-substituted thiazolidi-4-none, namely, (2E, 5Z)-3-(4-fluorophenyl)-2-(4-fluorophenylimino)-5-((E)-3-(2-nitrophenyl)allyliden) thiazolidin-4-one (F2NTh) was synthesized and characterized by several experimental spectroscopic techniques. SC-XRD has been employed to determine the crystalline structure of F2NTh, which crystallized in the monoclinic $P2_1/c$ space group. The geometry of F2NTh was optimized by using B3LYP and CAM-B3LYP functionals with the 6-311G(d,p) basis set. The calculated geometrical parameters were compared with experimental ones, showing a good agreement between both results. Along with the experimental characterization, the IR vibrational frequencies and NMR chemical shifts were calculated, assigned, and discussed. The findings revealed that the predicted and experimental chemical shift values, in general, were consistent. Furthermore, the structural study has shown the existence of some intermolecular interactions in the crystal packing of the title compound. These interactions are dominated by C–H···O and C–H···F hydrogen bonds. Using the Hirshfeld surface and its corresponding two-dimensional fingerprint, all the intercontacts were identified and their contributions calculated. Thus, the H···H contact interactions represent the most significant contribution to the HS of the title molecule, with 23.6%. The nocovalent and Van der Waals interactions were also investigated using RDG analysis. The considerable charge transfer interactions occurring within the molecule are explained by the computed HOMO-LUMO energy gap (3.086 eV with B3LYP and 5.830 eV with CAM-B3LYP) and the global chemical reactivity descriptors quantum parameters, which further support molecular stability. Hence, Fukui parameters indicate that fluorine atoms were identified as electrophilic sites. This last statement was confirmed by the MEP distribution, in which the elctrophilic sites are located on the fluorine and oxygen atoms and the nucleophilic sites are located on the hydrogen atoms of the phenyl rings. To describe the electron distribution throughout the title molecule, MPA, NPA, MC5, and ESP atomic charges were estimated. The findings of this analysis suggested that the title molecule is considered to have a significant electrophilic character, as confirmed by the high value of the electophilicity index of 7.875 eV. The theoretical UV-visible spectrum was computed using the TD-DFT method with both B3LYP and CAM-B3LYP functionals, and then it was compared against the experimental spectrum. The most intense peaks are assigned to n–π* and π–π* electronic transitions, and the experimental results are close to those of the CAM-B3LYP calculation. Thermodynamic properties were theoretically investigated and discussed. Finally, the static and dynamic NLO properties were investigated by calculating the electric dipole moment (μ), polarizability (α), and first and second hyperpolarizability (β and γ) using the B3LYP and CAM-B3LYP functionals. The obtained results revealed that, in comparison to previously studied materials, F2NTh exhibits significant NLO behavior.

Supplementary crystallographic data

CCDC 2287992 contains supplementary crystallographic data for this paper. These data can be obtained free of charge from The Cambridge Crystallographic Data Centre via www.ccdc.cam.ac.uk/data_request/cif, or by emailing data_request@ccdc.cam.ac.uk, or by contacting The Cambridge Crystallographic Data Centre, 12, Union Road, Cambridge CB2 1EZ, UK; Fax: +44 1223 336033.

Acknowledgments

This work was supported by the ministry of higher education and scientific research, the Directorate General for Scientific Research and Technological Development (DG-RSDT), and the Abdelhamid Ibn Badis University of Mostaganem.

CRediT authorship contribution statement

N. Kheddam: Methodology, Investigation, Writing - review & editing. A. Djafri: Synthesis, Writing - review & editing, Data curation. Y. Megrouss: Methodology, Investigation, Software, Writing - review & editing, Formal analysis. R. Rahmani: Investigation, Software, figures preparation. A. R. Guerroudj: X-ray Data Processing, Structure Determination, CIF validation. S. Belhachemi: Methodology, Investigation, Writing - review & editing. A. Djafri: Synthesis, Supervision, Spectroscopic analysis, reviewing. A. Chouaih: Supervision, Conceptualization, Methodology, review & editing.

Declaration of Competing Interest

The authors declare no conflict of interest.

References

[1] A. El Hallaoui, S. Chehab, B. Malek, O.Zimou, T. Ghailane, S. Boukhris, A. Souizi, R. Ghailane. « Valorization of the Modified Mono Ammonium Phosphate by Cobalt in the Synthesise of 3,4-Dihydropyrano[c]Chromene Derivatives ». *ChemistrySelect*. 4(11) (2019) 3062-70. https://doi.org/10.1002/slct.201803551

[2] S. Chehab, Y. Merroun, T. Ghailane, N. Habbadi, S. Boukhris, A. Hassikou, R. Ghailane, and al. « A New Process for $Na_2Ca(HPO_4)_2$ Synthesis and Its Application as a Heterogeneous Catalyst in Knoevenagel Condensation ». *Mediterr. J. Chem.* 7(1) (2018) 56-67. https://doi.org/10.13171/mjc71/01804111125-souizi

[3] Y. Merroun, S. Chehab, T. Ghailane, S. Boukhris, R. Ghailane, N. Habbadi, A. Hassikou, B. Lakhrissi, A. Souizi. « An Effective Method to Synthesize 2,3-Dihydroquinazolin-4(1H)- One Using Phosphate Fertilizers (MAP, DAP and TSP) as Green Heterogeneous Catalysts ». *J. Turk. Chem. Soc.* Section A: Chemistry 5(1) (2017) 303-16. https://doi.org/10.18596/jotcsa.363818

[4] S. Ferraa, Y. Merroun, H. Barebita, S. Cheha, B. Baach, A. Nimour, R. Ghailane, A. Souizi, T. Guedira. « Synthesis and characterization of Bi17Ba0,45V2,1-xPxO31,2 composite and their application as heterogeneous catalysts in biscoumarins derivatives synthesis ». *Results in Chemistry* 5 (2023) 100746. https://doi.org/10.1016/j.rechem.2022.100746

[5] S. Chehab, Y. Merroun, T. Ghailane, R. Ghailane, S. Boukhris, A. Souizi. « Mono-Ammonium Phosphate Fertilizer Modified by Cadmium: An Efficient and Recyclable Catalyst for 2,3-Dihydroquinazolin-4(1H)-One Derivatives Synthesis ». *Polycycl Aromat Compd.* 42(9) (2022) 6199-6214. https://doi.org/10.1080/10406638.2021.1977348

[6] A. El Hallaoui, T. Ghailane, S. Chehab, Y. Merroun, R. Ghailane, S. Boukhris, T. Guedira, A. Souizi. « Synthesis of New Bimetallic Phosphate (Al/Ag3PO4) and Study for Its Catalytic Performance in the Synthesis

of 1,2-Dihydro-l-Phenyl-3H-Naphth [1,2-e]-[1,3] Oxazin-3-One Derivatives ». *Mediterr. J. Chem*. 11(3) (2021) 215-28. http://dx.doi.org/10.13171/mjc02108091579elhallaoui

[7] Y. Merroun, S. Chehab, T. Ghailane, R. Ghailane, S. Boukhris, A. Hassikou, N. Habbadi, B. Lakhrissi, A. Souizi. « Comparative Study between the Titanium Phosphate TiP2O7 and the Phosphate Fertilizers in the Catalysis of the Quinazolin-4(3H)-One Derivatives Synthesis ». *Mediterr. J. Chem*. 10(6) (2020) 553-67. https://doi.org/10.13171/mjc106020201368ym

[8] S. Chehab, Y. Merroun, T. Ghailane, R. Ghailane, S. Boukhris, M. Akhazzane, A. Kerbal, A. Souizi. « Synthesis of 9-Arylhexahydroacridine-1,8-Diones Using Phosphate Fertilizers as Heterogeneous Catalysts ». *Russ. J. Org. Chem*. 55(9) (2019) 1380-86. https://doi.org/10.1134/S1070428019090185

[9] Y. Merroun, S. Chehab, A. El Hallaoui, T. Guedira, S. Boukhris, A. Souizi, R. Ghailane, A new heterogeneous catalyst of triple superphosphate/titanium tetrachloride is used for the synthesis of 1,8-dioxooctahydroxanthenes and tetrahydrobenzo[b]pyrans, *J. Mol. Struct.* 1294 (2023) 136554, https://doi.org/10.1016/j.molstruc.2023.136554

[10] S. Chehab, Y. Merroun, A. El Hallaoui, T. Ghailane, S. Boukhris, T. Guedira, R. Ghailane, A. Souizi. « Catalytic Performance of Cadmium Pyrophosphate in the Knoevenagel Condensation and One-Pot Multi Component Reaction of Chromene Derivatives ». *J. Chem. Sci.* 135(3) (2023) 95. https://doi.org/10.1007/s12039-023-02213-x

[11] Y. Merroun, S. Chehab, A. El Hallaoui, T. Guedira, S. Boukhris, R. Ghailane, A. Souizi. « Triple superphosphate modified by tin (II) chloride: As a reusable and efficient catalyst for the one-pot synthesis of xanthene and xanthenone derivatives under green conditions ». *J. Mol. Struct.* 1294 (2023) 136383. https://doi.org/10.1016/j.molstruc.2023.136383

[12] Y. Merroun, S. Chehab, A. Hallaoui, T. Guedira, S. Boukhris, R. Ghailane & A. Souizi. « Synthesis, Characterization, and Catalytic Application of SnP2O7 for the Highly Efficient Synthesis of Xanthene Derivatives ». *Polycycl Aromat Compd.* (2023) 1-15. https://doi.org/10.1080/10406638.2023.2247128

[13] A. El Hallaoui, Y. Merroun, S. Chehab, S. Boukhris, H. Hassoune, R. Ghailane, A. Souizi. « Efficient Synthesis of Symmetrically Substituted Pyridines and Substituted Alkenes through Green and Heterogeneous Catalysis with Zinc Phosphate ». *Org. Biomol. Chem.* 21(31) (2023) 6368-6378. https://doi.org/10.1039/D3OB00634D

[14] S. Chehab, Y. Merroun, R. Ghailane, S. Boukhris, A. Souizi. « Na_2Ca $(HPO_4)_2$, an Efficient, Reusable Eco-Friendly Catalyst for the Synthesis of 1,8-Dioxo-Octahydroxanthenes and Biscoumarin Derivatives ». *Polycycl Aromat Compd.* 43(6) (2023) 4906-4923. https://doi.org/10.1080/10406638.2022.2094421

[15] Y. Merroun, S. Chehab, A. El Hallaoui, R. Ghailane, S. Boukhris, A. Souizi. Tin pyrophosphate (SnP2O7): as a novel heterogeneous and highly efficient catalyst for the one pot-three component synthesis of Tetrahydrobenzo[b]pyran and Dihydropyran[c]chromene derivatives, Iranian Journal of Chemistry and Chemical Engineering, (2022). https://doi.org/10.30492/IJCCE.2022.562958.5619

[16] S. Chehab, Y. Merroun, T. Ghailane, R. Ghailane, S. Boukhris, B. Lakhrissi, A. Souizi. « A Facile and Efficient Synthesis of Tetrahydrobenzo[b]Pyrans and Dihydropyrano[4,3-b] Pyrans Derivatives Using Phosphate Fertilizers MAP, DAP, and TSP as Heterogeneous Catalysts ». *J. Iran. Chem. Soc.* 18(10) (2021) 2665-2678. https://doi.org/10.1007/s13738-021-02223-x

[17] Y. Merroun, S. Chehab, T. Ghailane, M. Akhazzane, A. Souizi, R. Ghailane. « Preparation of Tin-Modified Mono-Ammonium Phosphate Fertilizer and Its Application as Heterogeneous Catalyst in the Benzimidazoles and Benzothiazoles Synthesis ». *React. Kinet. Mech. Catal.* 126(1) (2019) 249-264. https://doi.org/10.1007/s11144-018-1446-5

[18] A. Souizi, S. Chehab, Y. Merroun, T. Ghailane, R. Ghailane, S. Boukhris. « A Green and Efficient Method for the Synthesis of 3,4- Dihydropyrano[c]Chromene Using Phosphate Fertilizers (MAP, DAP and TSP) as Heterogeneous Catalysts ». *J. Turk. Chem. Soc. Section A: Chemistry* 5(2) (2018) 355-370. https://doi.org/10.18596/jotcsa.358609

[19] N. Khelloul, K. Toubal, N. Boukabcha, N. Dege, A. Djafri, N.E.H. Belkafouf, N. Benhalima, A. Djafri, A. Chouaih, Y. Atalay, 2-thioxo -3N-(2-ethoxyphenyl) -5[4′-methyl -3′N-(2′-ethoxyphenyl) thiazol-2′(3′H)-ylidene] thiazolidin-4-one: Growth, spectroscopic behavior, single-crystal investigation, Hirshfeld surface analysis, DFT/TD-DFT computational studies and NLO evaluation, *Phosphorus Sulfur Silicon Relat. Elem.* 198(3) (2023) 199-214. https://doi.org/10.1080/10426507.2022.2134373.

[20] R. Rahmani, F. Perveen, N. Benhalima, A. Djafri, N. Khelloul, A. Chouaih, A. Djafri, M.B. Kanoun, S. Goumri-Said, FTIR, NMR and UV–visible spectral investigations, theoretical calculations, topological analysis, chemical stability, and molecular docking study on novel bioactive compound: the 5-(5-nitro furan-2-ylmethylen), 3-N-(2-methoxy phenyl),2-N′- (2-methoxyphenyl) imino thiazolidin-4-one, *Polycycl Aromat Compd.* 43:5 (2023) 4685–4706. https://doi.org/10.1080/10406638.2022.2094971.

[21] Y.O. Mekhlef, A.M. AboulMagd, A.M. Gouda, Design, synthesis, molecular docking, and biological evaluation of novel 2,3-diaryl-1,3-thiazolidine-4-one derivatives as potential anti-inflammatory and cytotoxic agents, *J. Bioorganic Chemistry*. (2023) 106411. https://doi.org/10.1016/j.bioorg.2023.106411.

[22] H.M.A. Abumelha, A. Saeed, Synthesis of some 5-arylidene-2-(4-acetamidophenylimino)-thiazolidin-4-one derivatives and exploring their breast anticancer activity, *J. Heterocycl. Chem.* 57 (2020) 1816–1824. https://doi.org/10.1002/jhet.3906.

[23] Ł. Popiołek, I. Piątkowska-Chmiel, M. Gawrońska-Grzywacz, A. Biernasiuk, M. Izdebska, M. Herbet, M. Sysa, A. Malm, J. Dudka, M. Wujec, New hydrazide-hydrazones and 1,3-thiazolidin-4-ones with 3-hydroxy-2-naphthoic moiety: Synthesis, in vitro and in vivo studies, *J. Biomed. Pharmacother.* 103 (2018) 1337–1347. https://doi.org/10.1016/j.biopha.2018.04.163.

[24] N. Kerru, L. Gummidi, S.V.H.S. Bhaskaruni, S.N. Maddila, S.B. Jonnalagadda, Ultrasound-assisted synthesis and antibacterial activity of novel 1,3,4-thiadiazole-1H-pyrazol-4-yl-thiazolidin-4-one derivatives, *J. Monatsh Chem.* 151 (2020) 981–990. https://doi.org/10.1007/s00706-020-02625-2.

[25] Y.K. Abhale, A. Shinde, M. Shelke, L. Nawale, D. Sarkar, P.C. Mhaske, Synthesis of new 2-(thiazol-4-yl)thiazolidin-4-one derivatives as potential anti-mycobacterial agents, *J. Bioorg. Chem*. 115 (2021) 105192. https://doi.org/10.1016/j.bioorg.2021.105192.

[26] N. Saini, A. Sharma, V.K. Thakur, C. Makatsoris, A. Dandia, M. Bhagat, R.K. Tonk, P.C. Sharma, Microwave assisted green synthesis of thiazolidin-4-one derivatives: A perspective on potent antiviral and antimicrobial activities*, J. CRGSC*. 3 (2020) 100021. https://doi.org/10.1016/j.crgsc.2020.100021.

[27] S.K. Pandey, U. Yadava, M.L. Sharma, A. Upadhyay, M.P. Gupt, A.R. Dwivedi, A. Khatoon, Synthesis, molecular structure investigation, biological evaluation and docking studies of novel spirothiazolidinones, *J. Results in Chem*. 5 (2023) 100726. https://doi.org/10.1016/j.rechem.2022.100726.

[28] A.D. Patel, T.Y. Pasha, P. Lunagariya, U. Shah, T. Bhambharoliya, R.K.P. Tripathi, A Library of Thiazolidin-4-one Derivatives as Protein Tyrosine Phosphatase 1B (PTP1B) Inhibitors: An Attempt To Discover Novel Antidiabetic Agents, *J. ChemMedChem*. 15 (2020) 1229–1242. https://doi.org/10.1002/cmdc.202000055.

[29] T.S. Chitre, S.M. Patil, A.G. Sujalegaonkar, K.D. Asgaonkar, Designing of Thiazolidin-4-one Pharmacophore using QSAR Studies for Anti-HIV Activity, *IJPER*. 55 (2021) 581–589. https://doi.org/10.5530/ijper.55.2.97.

[30] P. Roszczenko, S. Holota, O.K. Szewczyk, R. Dudchak, K. Bielawski, A. Bielawska, R. Lesyk, 4-Thiazolidinone-Bearing Hybrid Molecules in Anticancer Drug Design, *J. Int. J. Mol. Sci.* 23 (2022) 13135. https://doi.org/10.3390/ijms232113135.

[31] G. Ramesh, B. Rathnakar, C. Narsaiah, N. Rameshwar, M. Srinivas, V. Namratha, G. Durgaiah, Y.N. Reddy, B.V. Reddy, M. Satyanarayana, Synthesis, DFT computations, molecular docking studies and anticancer activity of 2-(4-fluorophenyl)-3-(5-methylisoxazol-3-yl)thiazolidin-4-one, Chemical Data Collections. 39 (2022) 100859. https://doi.org/10.1016/j.cdc.2022.100859.

[32] R. Rahmani, A. Djafri, J.-C. Daran, A. Djafri, A. Chouaih, F. Hamzaoui, Crystal structure of (2Z,5Z)-3-(4-methoxyphenyl)-2-[(4-methoxyphenyl)imino]-5-[(E)-3-(2-nitro-phenyl) allylidene]-1,3-thiazolidin-4-one, *Acta Cryst. E*72 (2016) 155-157. https://doi.org/10.1107/S2056989016000207.

[33] T. A. Schaub, K. Padberg, M. Kivala, Bridged triarylboranes, -silanes, -amines, and - phosphines as minimalistic heteroatom-containing polycyclic aromatic hydrocarbons: Progress and challenges, *J. Phys. Org. Chem.* 33 (2020) 4022-4049. https://doi.org/10.1002/poc.4022

[34] A.D. Becke, Density-functional thermochemistry. III. The role of exact exchange, *J. Chem. Phys.* 98 (1993) 5648–5652. https://doi.org/10.1063/1.464913.

[35] C. Lee, W. Yang, and R. G. Parr, "Development of the Colle-Salvetti Correlation-Energy Formula into a Functional of the Electron Density," Physical Review B, Condensed Matter 37, no. 2 (1988): 785–9. https://doi.org/10.1103/PhysRevB.37.785.

[36] A. Nekrouf, K. Toubal, Y. Megrouss, N.E.H. Belkafouf, A. Djafri, N. Khelloul, J.-C. Daran, A. Djafri, A. Chouaih, Synthesis, structural, spectroscopic, intermolecular interactions, kinetic stability, charge transfer method with DNA bases and electronic properties of (E)-3-(2-ethoxyphenyl)-5-(3-(2-methoxyphenyl)-4methylthiazol-2(3H)-ylidene)-2thioxothiazolidin-4-one: Computational and experimental approach, *J. Mol. Struct.* 1262 (2022) 133002. https://doi.org/10.1016/j.molstruc.2022.133002.

[37] A. Djafri, A. Chouaih, J.-C. Daran, A. Djafri, F. Hamzaoui, Crystal and molecular structure of (2Z,5Z)-3-(2-meth-oxy-phen-yl)-2-[(2-meth-oxy-phen-yl)imino]-5-(4-nitro-benzyl-idene)thia-zolidin-4-one, *Acta Cryst. E.* 73 (2017) 511–514. https://doi.org/10.1107/S2056989017003218.

[38] R. Rahmani, A. Djafri, A. Chouaih, A. Djafri, F. Hamzaoui, R. Rizzi, A. Altomare, Synthesis, molecular and solid state structure of 5-(5-nitro furan-2-ylmethylen), 3-N-(2-methoxy phenyl), 2-N′-(2-methoxyphenyl) imino thiazolidin-4-one: X-ray powder diffraction and DFT studies, *J. Mol. Struct*. 1143, (2017) 259–264. https://doi.org/10.1016/j.molstruc.2017.04.091.

[39] I.K. Petrushenko, K.B. Petrushenko, Effect of methyl substituents on the electronic transitions in simple meso-aniline-BODIPY based dyes: RI-CC2 and TD-CAM-B3LYP computational investigation, *Spectrochim. Acta - A: Mol. Biomol*. 190 (2018) 239–245. https://doi.org/10.1016/j.saa.2017.09.025.

[40] Z.D. Benyahlou, F. Triki-Baara, S. Yahiaoui, Y. Megrouss, N. Boukabcha, A. Djafri, A. Chouaih, A. Hatzidimitriou, Synthesis, crystal structure, Hirshfeld surface, energy framework, NCI-RDG, theoretical

calculations and molecular docking of (Z)-4,4′-bis[-3-N-ethyl-2-N'-(phenylimino) thiazolidin-4-one] methane, *J. Mol. Struct*. 1277 (2023) 134781. https://doi.org/10.1016/j.molstruc.2022.134781.

[41] T. Yanai, D.P. Tew, N.C. Handy, A new hybrid exchange–correlation functional using the Coulomb-attenuating method (CAM-B3LYP), *J. Chem. Phys.* Lett. 393 (2004) 51–57. https://doi.org/10.1016/j.cplett.2004.06.011.

[42] D.D. Nguyen, N.C. Jones, S.V. Hoffmann, J. Spanget–Larsen, Near and vacuum UV polarization spectroscopy of 1,4-distyrylbenzene, *J. Spectrochim. Acta A Mol. Biomol.* 286 (2023) 122019. https://doi.org/10.1016/j.saa.2022.122019.

[43] M. Iqbal, A. Hussain, A. Naz, R. Hussain, M. Yar, K. Ayub, M.R.H. Shah Gilani, M. Imran, M.A. Assiri, Tailoring the solar cell efficiency of Y-series based non-fullerene acceptors through end cap modification, *J. Spectrochim. Acta A Mol. Biomol.* 291 (2023) 122322. https://doi.org/10.1016/j.saa.2023.122322.

[44] G.M. Sheldrick, A short history of SHELX, *Acta Crystallographica Section A Foundations of Crystallography*. 64 (2008) 112–122. https://doi.org/10.1107/S0108767307043930.

[45] G.M. Sheldrick, Crystal structure refinement with SHELXL, *Acta Crystallographica Section C Structural Chemistry*. 71 (2015) 3–8. https://doi.org/10.1107/S2053229614024218.

[46] L.J. Farrugia, WinGX and ORTEP for Windows: an update, *J Appl Cryst.* 45 (2012) 849–854. https://doi.org/10.1107/S0021889812029111.

[47] C.F. Macrae, P.R. Edgington, P. McCabe, E. Pidcock, G.P. Shields, R. Taylor, M. Towler, J. van de Streek, Mercury: visualization and analysis of crystal structures, *J. Appl Cryst.* 39 (2006) 453–457. https://doi.org/10.1107/S002188980600731X.

[48] M. Nardelli, PARST95 – an update to PARST: a system of Fortran routines for calculating molecular structure parameters from the results of crystal structure analyses, *J. Appl Cryst.* 28 (1995) 659–659. https://doi.org/10.1107/S0021889895007138.

[49] M.A. Spackman, D. Jayatilaka, Hirshfeld surface analysis, *J. Cryst.Eng.Comm*. 11 (2009) 19–32. https://doi.org/10.1039/B818330A.

[50] M.J. Frisch, G.W. Trucks, H.B. Schlegel, G.E. Scuseria, M.A. Robb, J.R. Cheeseman, G. Scalmani, V. Barone, B. Mennucci, G.A. Petersson, H. Nakatsuji, M. Caricato, X. Li, H. P. Hratchian, A.F. Izmaylov, J. Bloino, G. Zheng, J.L. Sonnenberg, M. Hada, M. Ehara, K. Toyota, R. Fukuda, J. Hasegawa, M. Ishida, T. Nakajima, Y. Honda, O. Kitao, H. Nakai, T. Vreven, J.A.Jr. Montgomery, J.E. Peralta, F. Ogliaro, M. Bearpark, J.J. Heyd, E. Brothers, K.N. Kudin, V.N. Staroverov, R. Kobayashi, J. Normand, K. Raghavachari, A. Rendell, J. C. Burant, S.S. Iyengar, J. Tomasi, M. Cossi, N. Rega, J.M. Millam, M. Klene, J.E. Knox, J.B. Cross, V. Bakken, C. Adamo, J. Jaramillo, R. Gomperts, R.E. Stratmann, O. Yazyev, A.J. Austin, R. Cammi, C. Pomelli, J.W. Ochterski, R.L. Martin,; K. Morokuma, V.G. Zakrzewski, G.A. Voth, P. Salvador, J.J. Dannenberg, S. Dapprich, A.D. Daniels, Ö. Farkas, J.B. Foresman, J.V. Ortiz, J. Cioslowski, D.J. Fox, Gaussian 09, Revision A. 02. *Gaussian, Inc.*, Pittsburgh PA, (2009).

[51] Dennington, R., Keith, T. and Millam, J. (2009) Gauss View, Version 5. *Semichem Inc.*, Shawnee Mission.

[52] M.H. Jamróz, Vibrational Energy Distribution Analysis (VEDA): Scopes and limitations, *J. Spectrochim. Acta A Mol. Biomol*. *Spectrosc.*114 (2013) 220–230. https://doi.org/10.1016/j.saa.2013.05.096.

[53] K. Wolinski, J.F. Hinton, P. Pulay, Efficient implementation of the gauge-independent atomic orbital method for NMR chemical shift calculations, *J. Am. Chem. Soc.* 112 (1990) 8251–8260. https://doi.org/10.1021/ja00179a005.

[54] T. Lu, F. Chen, Multiwfn: A multifunctional wave function analyzer, *J. Comput. Chem.* 33 (2012) 580–592. https://doi.org/10.1002/jcc.22885.

[55] W. Humphrey, A. Dalke, K. Schulten, VMD: Visual molecular dynamics, J.Mol. Graph. 14 (1996) 33–38. https://doi.org/10.1016/0263-7855(96)00018-5.

[56] S. Canneaux, F. Bohr, E. Henon, KiSThelP: A program to predict thermodynamic properties and rate constants from quantum chemistry results†, *J. Comput. Chem.* 35 (2014) 82–93. https://doi.org/10.1002/jcc.23470.

[57] I. Singh, A.A. El-Emam, S.K. Pathak, R. Srivastava, V.K. Shukla, O. Prasad, L. Sinha, Experimental and theoretical DFT (B3LYP, X3LYP, CAM-B3LYP and M06-2X) study on electronic structure, spectral features, hydrogen bonding and solvent effects of 4-methylthiadiazole-5-carboxylic acid, *J. Mol Simul.* 45 (2019) 1029–1043. https://doi.org/10.1080/08927022.2019.1629434.

[58] A.M. Al-Majid, S.M. Soliman, H.A. Ghabbour, M. Ali, M.S. Islam, M.R. Shaik, A. Barakat, Synthesis and X-ray crystal structure of unexpected novel thiazolidinone/1,3,4-thiadiazole heterocycle via S-alkylation and Smiles rearrangement dual approaches, *J. Mol. Struct.* 1234 (2021) 130156. https://doi.org/10.1016/j.molstruc.2021.130156.

[59] A.R. Guerroudj, N. Boukabcha, A. Benmohammed, N. Dege, N.E.H. Belkafouf, N. Khelloul, A. Djafri, A. Chouaih, Synthesis, crystal structure, vibrational spectral investigation, intermolecular interactions, chemical reactivity, NLO properties and molecular docking analysis on (E)-N-(4-nitrobenzylidene)-3-chlorobenzenamine:

A combined experimental and theoretical study, *J. Mol. Struct*. 1240 (2021) 130589. https://doi.org/10.1016/j.molstruc.2021.130589.

[60] E. Bravanjalin Subi, D. Arul Dhas, S. Balachandran, I. Hubert Joe, Crystal Growth, Structural, Vibrational, Effects of Hydrogen Bonding (C-H…O and C-H…N), Chemical Reactivity, Antimicrobial Activity, Inhibitory Effects and Molecular Dynamic Simulation of 4-Methoxy-N-(Nitrobenzylidene)-Aniline, *Polycycl. Aromat. Compd*. (2022) 1–55. https://doi.org/10.1080/10406638.2022.2052116.

[61] N. Benhalima, S. Yahiaoui, N. Boubegra, M. Boulakoud, Y. Megrouss, A. Chouaih, F. Hamzaoui, Quantum chemical investigation of spectroscopic, electronic and NLO properties of (1E, 4E)-1-(3-nitrophenyl)-5-phenylpenta-1, 4-dien-3-one, *Int. J. Adv. Chem.* 6 (2018) 121–131.

[62] M.H.M. Belhachemi, A. Benmohammed, H. Saiah, N. Boukabcha, M. Saidj, N. Dege, A. Djafri, A. Chouaih, Synthesis, structural determination, molecular docking and biological activity of 1-(4-fluorobenzyl)-5-bromolindolin-2,3-dione, *J. Mol. Struct*. 1265 (2022) 133342. https://doi.org/10.1016/j.molstruc.2022.133342.

[63] M. Yaman, E. Aydemir, N. Dege, E. Agar, T.S. Iskenderov, Synthesis, crystallographic analysis and Hirshfeld surface analysis of 4-bromo-2-{[2-(5-bromo-2-nitro-phen-yl)hydrazin-1-yl-idene]meth-yl}-5-fluoro-phenol, *Acta Crystallogr E Crystallogr Commun*. 74 (2018) 1628–1632. https://doi.org/10.1107/S2056989018014627.

[64] E.G. COX, Crystal Structure of Benzene, *J. Rev. Mod. Phys.* 30 (1958) 159–162. https://doi.org/10.1103/RevModPhys.30.159.

[65] M. Saidj, A. Djafri, R. Rahmani, N.E.H. Belkafouf, N. Boukabcha, A. Djafri, A. Chouaih, Molecular Structure, Experimental and Theoretical Vibrational Spectroscopy, (HOMO-LUMO, NBO) Investigation, (RDG, AIM) Analysis, (MEP, NLO) Study and Molecular Docking of Ethyl-2-[4-Ethyl-5-(Quinolin-8-yloxyMethyl)-4H-1,2,4-Triazol-3-yl] Sulfanyl Acetate, *J. Polycycl Aromat Compd*. 43:3 (2023) 2152–2176. https://doi.org/10.1080/10406638.2022.2039238.

[66] R. Srivastava, F.A.M. Al-Omary, A.A. El-Emam, S.K. Pathak, M. Karabacak, V. Narayan, S. Chand, O. Prasad, L. Sinha, A combined experimental and theoretical DFT (B3LYP, CAM-B3LYP and M06-2X) study on electronic structure, hydrogen bonding, solvent effects and spectral features of methyl 1H-indol-5-carboxylate, *J. Mol. Struct.* 1137 (2017) 725–741. https://doi.org/10.1016/j.molstruc.2017.02.084.

[67] J.B. Lambert, H.F. Shurvell, L.R. Verbit, R.G. Cooks, G.H. Stout, Organic structural analysis, *Macmillan Publishing Company*, 1976.

[68] M. Azayez, S. Chetioui, Y. Megrouss, N. Boukabcha, A. Djedouani, A.R. Guerroudj, N. Meddah Araibi, A. Chouaih, Experimental and theoretical spectroscopic characterization, Hirshfeld surface analysis, TD-DFT calculation, and nonlinear optical properties of (E)-1-[(2,4,6tribromophenyl)diazenyl]-naphthalen-2-ol azo dye, *J. Mol. Struct*. 1261 (2022) 132887. https://doi.org/10.1016/j.molstruc.2022.132887.

[69] A. Djafri, F. Perveen, N. Benhalima, N. Khelloul, R. Rahmani, A. Djafri, A. Chouaih, M.B. Kanoun, S. Goumri-Said, Experimental spectral characterization, Hirshfeld surface analysis, DFT/TD-DFT calculations and docking studies of (2Z,5Z)-5-(4-nitrobenzylidene)-3-N(2-methoxyphenyl)-2-N’(2-methoxyphenylimino) thiazolidin-4-one, *Heliyon*. 6 (2020). https://doi.org/10.1016/j.heliyon.2020.e05754.

[70] M.M. Ismail, G.M. Morsy, H.M. Mohamed, M.A.M. El-Mansy, M.M.A. Abd-Alrazk, FT-IR spectroscopic analyses of 4-hydroxy-1-methyl-3-[2-nitro-2-oxoacetyl-2(1H)quinolinone (HMNOQ), *J. Spectrochim. Acta A Mol. Biomol. Spectrosc.* 113 (2013) 191–195. https://doi.org/10.1016/j.saa.2013.04.117.

[71] G. Liu, Q. Fang, W. Xu, H. Chen, C. Wang, Vibration assignment of carbon–sulfur bond in 2-thione-1,3-dithiole-4,5-dithiolate derivatives, *J. Spectrochim. Acta A Mol. Biomol. Spectrosc.* 60 (2004) 541–550. https://doi.org/10.1016/S1386-1425(03)00260-9.

[72] B.A. Trofimov, L.M. Sinegovskaya, N.K. Gusarova, Vibrations of the S–S bond in elemental sulfur and organic polysulfides: a structural guide, *J. Sulphur Chem*. 30 (2009) 518–554. https://doi.org/10.1080/17415990902998579.

[73] N.E.H. Belkafouf, F. Triki-Baara, A. Altomare, R. Rizzi, A. Chouaih, A. Djafri, F. Hamzaoui, Synthesis, PXRD structural determination, Hirshfeld surface analysis and DFT/TD-DFT investigation of 3N-ethyl-2N’-(2-ethylphenylimino) thiazolidin-4-one, *J. Mol. Struct.* 1189 (2019) 8–20. https://doi.org/10.1016/j.molstruc.2019.04.028.

[74] C. Tabti, A. Benmohammed, N. Boukabcha, N. Dege, A. Djafri, F.Z. Boudjenane, A. Chouaih, A. Djafri, Synthesis, Structural Characterization and Theoretical NLO Activity of N-(4-Acetyl-5-(4-(Nitro) Phenyl)-4,5-Dihydro-1,3,4-Thiadiazol-2-yl)-N-Phenyl Acetamide, *Polycycl Aromat Compd.* (2022) 1–22. https://doi.org/10.1080/10406638.2022.2158882.

[75] P. Chawla, R. Singh, S.K. Saraf, Effect of chloro and fluoro groups on the antimicrobial activity of 2,5-disubstituted 4-thiazolidinones: a comparative study, *J. Med Chem Res.* 21 (2012) 3263–3271. https://doi.org/10.1007/s00044-011-9864-1.

[76] C.M. Widdifield, S.O.N. Lill, A. Broo, M. Lindkvist, A. Pettersen, A.S. Ankarberg, P. Aldred, S. Schantz, L. Emsley, Does Z′ equal 1 or 2? Enhanced powder NMR crystallography verification of a disordered

room temperature crystal structure of a p38 inhibitor for chronic obstructive pulmonary disease, *Phys. Chem. Chem. Phys.* 19 (2017) 16650–16661. https://doi.org/10.1039/C7CP02349A.

[77] S. Yahiaoui, A. Moliterni, N. Corriero, C. Cuocci, K. Toubal, A. Chouaih, A. Djafri, F. Hamzaoui, 2-thioxo- 3N-(2-methoxyphenyl) −5 [4′-methyl -3′N -(2′-methoxyphenyl) thiazol-2′(3′H)-ylidene] thiazolidin-4-one: Synthesis, characterization, X-ray single crystal structure investigation and quantum chemical calculations, *J. Mol. Struct.* 1177 (2019) 186–192. https://doi.org/10.1016/j.molstruc.2018.09.052.

[78] S.J. Grabowski, ed., Hydrogen Bonding-New Insights, *Springer Netherlands*, 2006. https://doi.org/10.1007/978-1-4020-4853-1.

[79] N. G. Garrison, S. A. Harry, M. A. Siegler, G. Cariello, R. A. Cormanich, T. Lectka, The CF···HCF2 interaction: A combination of hydrogen bonding and n → σ* stabilization, *J. Fluor. Chem.* 272 (2023) 110191. https://doi.org/10.1016/j.jfluchem.2023.110191

[80] M. Jini Pramila, D. Arul Dhas, I. Hubert Joe, S. Balachandran, G. Vinitha, Structural insights, spectral, flourescence, Z-scan, C-H…O/N-H…O hydrogen bonding and AIM, RDG, ELF, LOL, FUKUI analysis, NLO activity of N-2(Methoxy phenyl) acetamide, *J. Mol. Struct.* 1272 (2023) 134140. https://doi.org/10.1016/j.molstruc.2022.134140.

[81] M.A. Spackman, D. Jayatilaka, Hirshfeld surface analysis, *J. Cryst Eng Comm*. 11 (2009) 19–32. https://doi.org/10.1039/B818330A.

[82] K. Toubal, N. Boukabcha, Ö. Tamer, N. Benhalima, S. Altürk, D. Avcı, A. Chouaih, Y. Atalay, A. Djafri, F. Hamzaoui, Spectroscopic (FT-IR,1H and 13C NMR) characterization and density functional theory calculations for (Z)-5-(4-nitrobenzyliden)-3-N(2-ethoxyphenyl)-2-thioxo-thiazolidin-4-one (ARNO), J. Mol. Struct, 1147 (2017) 569–581. https://doi.org/10.1016/j.molstruc.2017.06.102.

[83] F.L. Hirshfeld, Bonded-atom fragments for describing molecular charge densities, *J. Theoret. Chim. Acta*. 44 (1977) 129–138. https://doi.org/10.1007/BF00549096.

[84] R. Arulraj, S. Sivakumar, K. Rajkumar, J.P. Jasinski, M. Kaur, A. Thiruvalluvar, Synthesis, Crystal Structure, DFT Calculations and Hirshfeld Surface Analysis of 3-Chloro-3-methyl-r(2),c(6)-bis(p-methoxyphenyl)piperidin-4-one, *J. Chem Crystallogr.* 50 (2020) 41–51. https://doi.org/10.1007/s10870-018-0759-6.

[85] G. Saleh, C. Gatti, L. Lo Presti, Non-covalent interaction via the reduced density gradient: Independent atom model vs experimental multipolar electron densities, *J. Comput. Theor. Chem*. 998 (2012) 148–163. https://doi.org/10.1016/j.comptc.2012.07.014.

[86] J.J. McKinnon, D. Jayatilaka, M.A. Spackman, Towards quantitative analysis of intermolecular interactions with Hirshfeld surfaces, *J. Chem. Commun.* (2007) 3814–3816. https://doi.org/10.1039/B704980C.

[87] B. Xu, J. Deng, X. Ding, J. Sun, J.Z. Liu, Van der Waals force-induced intralayer ferroelectric-to-antiferroelectric transition via interlayer sliding in bilayer group-IV monochalcogenides, *Npj Comput Mater*. 8 (2022) 1–9. https://doi.org/10.1038/s41524-022-00724-8.

[88] C. Chiter, A. Bouchama, T.N. Mouas, H. Allal, M. Yahiaoui, I. Warad, A. Zarrouk, A. Djedouani, Synthesis, crystal structure, spectroscopic and Hirshfeld surface analysis, NCI-RDG, DFT computations and antibacterial activity of new asymmetrical azines, *J. Mol. Struct.* 1217 (2020) 128376. https://doi.org/10.1016/j.molstruc.2020.128376.

[89] B. Silvi, A. Savin, Classification of chemical bonds based on topological analysis of electron localization functions, *Nature*. 371 (1994) 683–686. https://doi.org/10.1038/371683a0.

[90] A. Demirpolat, F. Akman, A.S. Kazachenko, An Experimental and Theoretical Study on Essential Oil of Aethionema sancakense: Characterization, Molecular Properties and RDG Analysis, *Molecules*. 27 (2022) 6129. https://doi.org/10.3390/molecules27186129.

[91] O. Kourat, A. Djafri, N. Benhalima, Y. Megrouss, N.E.H. Belkafouf, R. Rahmani, J.-C. Daran, A. Djafri, A. Chouaih, Synthesis, crystal structure, Hirshfeld surface analysis, spectral characterization, reduced density gradient and nonlinear optical investigation on (E)-N'-(4-nitrobenzylidene)-2-(quinolin-8-yloxy) acetohydrazide monohydrate: A combined experimental and DFT approach, *J. Mol. Struct.* 1222 (2020) 128952. https://doi.org/10.1016/j.molstruc.2020.128952.

[92] Y. Tao, L. Han, Y. Han, Z. Liu, A combined experimental and theoretical analysis on molecular structure and vibrational spectra of 2,4-dihydroxybenzoic acid, *J. Spectrochim Acta A Mol Biomol Spectrosc*. 137 (2015) 1078–1085. https://doi.org/10.1016/j.saa.2014.08.151.

[93] W.B. Davis, W.A. Svec, M.A. Ratner, M.R. Wasielewski, Molecular-wire behaviour in p-phenylenevinylene oligomers, *Nature*. 396 (1998) 60–63.

[94] N. Günay, H. Pir, D. Avcı, Y. Atalay, NLO and NBO Analysis of Sarcosine-Maleic Acid by Using HF and B3LYP Calculations, *J. Chem.* 2013 (2012) e712130. https://doi.org/10.1155/2013/712130.

[95] R.F.W. Bader, R.F.W. Bader, Atoms in Molecules: A Quantum Theory, Oxford *University Press*, Oxford, New York, 1994.

[96] I. Fleming, Frontier Orbitals and Organic Chemical Reactions 1976, *Willey and Sons, London*. (1982).

[97] F. El-Kalai, E. B. Çınar, C.-H. Lai, S. Daoui, T. Chelfi, M. Allali, N. Dege, K. Karrouchi, N. Benchat, Synthesis, spectroscopy, crystal structure, TGA/DTA study, DFT and molecular docking investigations of (E)-4-(4-methylbenzyl)-6-styrylpyridazin-3(2H)-one, *J. Mol. Struct.* 1228 (2021) 129435. https://doi.org/10.1016/j.molstruc.2020.129435.

[98] B.J. Powell, T. Baruah, N. Bernstein, K. Brake, R.H. McKenzie, P. Meredith, M.R. Pederson, A first-principles density-functional calculation of the electronic and vibrational structure of the key melanin monomers, *J. Chem Phys.* 120 (2004) 8608–8615. https://doi.org/10.1063/1.1690758.

[99] P. Thanikaivelan, V. Subramanian, J. Raghava Rao, B. Unni Nair, Application of quantum chemical descriptor in quantitative structure activity and structure property relationship, *J. Chemical Physics Letters*. 323 (2000) 59–70. https://doi.org/10.1016/S0009-2614(00)00488-7.

[100] R. Rahmani, A. Djafri, A. Chouaih, A. Djafri, F. Hamzaoui, A. Krallafa, Molecular Structure, FT-IR, NMR (13C/1H), UV-Vis Spectroscopy and DFT Calculations on (2Z, 5Z)-3-N'(4-Methoxy phenyl)-2-N'(4-methoxy phenyl imino)-5-((E)-3-(2-nitrophenyl)allylidene) thiazolidin-4-one, *S. Afr. J. Chem.* 72 (2019) 176–188. https://doi.org/10.17159/0379-4350/2019/v72a23.

[101] M. Momeni, H. Yousefi Mashhour, M.M. Kalantarian, New approaches to consider electrical properties, band gaps and rate capability of same-structured cathode materials using density of states diagrams: Layered oxides as a case study, *J. Alloys Compd*. 787 (2019) 738–743. https://doi.org/10.1016/j.jallcom.2019.02.155.

[102] N.M. O'boyle, A.L. Tenderholt, K.M. Langner, cclib: A library for package-independent computational chemistry algorithms, *J. Comput. Chem.* 29 (2008) 839–845. https://doi.org/10.1002/jcc.20823.

[103] M.S. Thippeswamy, L. Naik, C.V. Maridevarmath, G.H. Malimath, A comprehensive studies on photophysical and electrochemical properties of novel D-π-A thiophene substituted 1,3,4-oxadiazole derivatives for optoelectronic applications: A computational and experimental approach, *Chemical Physics.* 550 (2021) 111301. https://doi.org/10.1016/j.chemphys.2021.111301.

[104] V.S. Jeba Reeda, V. Bena Jothy, Vibrational spectroscopic, quantum computational (DFT), reactivity (ELF, LOL and Fukui), molecular docking studies and molecular dynamic simulation on (6-methoxy-2-oxo-2H-chromen-4-yl) methyl morpholine-4-carbodithioate, *J. Mol. Liq.* 371 (2023) 121147. https://doi.org/10.1016/j.molliq.2022.121147.

[105] M.A.S. Sakr, F.F. Sherbiny, A.-A.Sh. El-Etrawy, Hydrazone-based Materials; DFT, TD-DFT, NBO Analysis, Fukui Function, MESP Analysis, and Solar Cell Applications, *J Fluoresc*. 32 (2022) 1857–1871. https://doi.org/10.1007/s10895-022-03000-6.

[106] Ö. Tamer, M.H. Bhatti, U. Yunus, D. Avcı, Y. Atalay, M. Nadeem, S.R. Shah, M. Helliwell, Structural, spectroscopic, nonlinear optical and electronic properties of calcium N-phthaloylglycinate: A combined experimental and theoretical study, *J. Mol. Struct.* 1125 (2016) 315–322. https://doi.org/10.1016/j.molstruc.2016.06.084.

[107] R.S. Mulliken, Electronic Population Analysis on LCAO–MO Molecular Wave Functions. I, *J. Chem. Phys*. 23 (1955) 1833–1840. https://doi.org/10.1063/1.1740588.

[108] C.C. Ersanli, G. Kaya Kantar, S. Şaşmaz, Crystallographic, spectroscopic (FTIR and NMR) and quantum computational calculation studies on bis(2-methoxy-4-((E)-prop-1-enyl)phenyl)oxalate, J. Mol. Struct. 1143 (2017) 318–327. https://doi.org/10.1016/j.molstruc.2017.04.032.

[109] A.-S. Badran, M.A. Ibrahim, Synthesis, spectral characterization, DFT and in silico ADME studies of the novel pyrido[1,2-a]benzimidazoles and pyrazolo[3,4-b]pyridines, *J. Mol. Struct*. 1274 (2023) 134454. https://doi.org/10.1016/j.molstruc.2022.134454.

[110] P. Bultinck, C. Van Alsenoy, P.W. Ayers, R. Carbó-Dorca, Critical analysis and extension of the Hirshfeld atoms in molecules, *J. Chem. Phys.* 126 (2007) 144111. https://doi.org/10.1063/1.2715563.

[111] E. Sigfridsson, U. Ryde, Comparison of methods for deriving atomic charges from the electrostatic potential and moments, *J. Comput. Chem.* 19 (1998) 377–395. https://doi.org/10.1002/(SICI)1096-987X(199803)19:4<377::AID-JCC1>3.0.CO;2-P.

[112] M. Drissi, Y. Megrouss, N. Benhalima, R. Rahmani, A. Chouaih, F. Hamzaoui, Theoretical and Experimental Electrostatic Potential around the m-Nitrophenol Molecule, *Molecules*, 20:3 (2015) 4042-4054. https://doi.org/10.3390/molecules20034042.

[113] G. Durgadevi, V. Arjunan, S. Thirunarayanan, M.K. Marchewka, S. Mohan, Structure, electronic, spectroscopic and reactivity investigations of pharmacologically active compound 1–acetyl–3–indolecarboxaldehyde – An experimental and theoretical approach, *J. Mol. Struct*. 1164 (2018) 57–69. https://doi.org/10.1016/j.molstruc.2018.03.045.

[114] R.G. Parr, W. Yang, Density functional approach to the frontier-electron theory of chemical reactivity, *J. Am. Chem. Soc.* 106 (1984) 4049–4050. https://doi.org/10.1021/ja00326a036.

[115] M. Yahya, N. Seferoğlu, G. Kaplan, Y. Nural, A. Barsella, Z. Seferoğlu, Synthesis, nonlinear optical properties, photophysical, and theoretical studies of azo dye bearing coumarin-thiophene, *J. Mol. Struct*. 1273 (2023) 134257. https://doi.org/10.1016/j.molstruc.2022.134257.

[116] R. Satheeshkumar, K. Prabha, K.N. Vennila, K. Sayin, E. Güney, W. Kaminsky, R. Acevedo, Spectroscopic (FT-IR, NMR, single crystal XRD) and DFT studies including FMO, Mulliken charges, and Hirshfeld surface analysis, molecular docking and ADME analyses of 2-amino-4′-fluorobenzophenone (FAB), *J. Mol. Struct.* 1267 (2022) 133552. https://doi.org/10.1016/j.molstruc.2022.133552.

[117] J.J. Philips, M.A. Hudspeth, P.M. Browne, J.E. Peralta, Basis set dependence of atomic spin populations, *Chem. Phys. Lett*. 495 (2010) 146–150. https://doi.org/10.1016/j.cgplett.2010.06.046.

[118] R. Yankova, I. Tankov, NLO response as a function of structural water presence: A comparative experimental (UV-vis) and DFT (structural, NPA, MEP) study on $Cs_2Ni(SeO_4)_2$•$4H_2O$ and $Cs_2Ni(SeO_4)_2$, *J. Mol. Struct.* 1224 (2021) 129047. https://doi.org/10.1016/j.molstruc.2020.129047.

[119] A.V. Marenich, S.V. Jerome, C.J. Cramer, D.G. Truhlar, Charge Model 5: An Extension of Hirshfeld Population Analysis for the Accurate Description of Molecular Interactions in Gaseous and Condensed Phases, *J Chem Theory Comput.* 8 (2012) 527–541. https://doi.org/10.1021/ct200866d.

[120] O. Fizer, M. Fizer, V. Sidey, Y. Studenyak, R. Mariychuk, Benchmark of different charges for prediction of the partitioning coefficient through the hydrophilic/lipophilic index, *J Mol Model*. 24 (2018) 141. https://doi.org/10.1007/s00894-018-3692-x.

[121] C. Cárdenas, N. Rabi, P.W. Ayers, C. Morell, P. Jaramillo, P. Fuentealba, Chemical Reactivity Descriptors for Ambiphilic Reagents: Dual Descriptor, Local Hypersoftness, and Electrostatic Potential, *J. Phys. Chem.* A. 113 (2009) 8660–8667. https://doi.org/10.1021/jp902792n.

[122] M. Kour, S. Kumar, A. Feddag, S. Andotra, A. Chouaih, V.K. Gupta, R. Kant, S.K. Pandey, Synthesis, characterization, single crystal X-ray and DFT analysis of disubstituted phosphorodithioates, *J. Mol. Struct.* 1157 (2018) 708–715. https://doi.org/10.1016/j.molstruc.2017.12.103.

[123] S.K. Khalaf, Q.M.A. Hassan, C.A. Emshary, H.A. Sultan, Concentration effect on optical properties and optical limiting of PVA doped with nigrosin films, *J. Photochem. Photobiol. A*. 427 (2022) 113809. https://doi.org/10.1016/j.jphotochem.2022.113809.

[124] B. Brahmaji, P. Viswarupachary, N. Sivaganga Kumari, L. Santosh Kumar, K. Ramchandra Rao, Idiosyncratic photoluminescence of europium added sulfamic acid single crystal a potential NLO material for optoelectronics and devise applications, *J. Lumin.* 257 (2023) 119649. https://doi.org/10.1016/j.jlumin.2022.119649.

[125] R. Rahmani, N. Boukabcha, A. Chouaih, F. Hamzaoui, S. Goumri-Said, On the molecular structure, vibrational spectra, HOMO-LUMO, molecular electrostatic potential, UV–Vis, first order hyperpolarizability, and thermodynamic investigations of 3-(4-chlorophenyl)-1-(1yridine-3-yl) prop-2-en-1-one by quantum chemistry calculations, *J. Mol. Struct*. 1155 (2018) 484-495. https://doi.org/10.1016/j.molstruc.2017.11.033.

[126] A. Chouaih, F. Hamzaoui, G. Vergoten, Capability of X-ray diffraction to the determination of the macroscopic linear susceptibility in a crystalline environment: the case of 3-Methyl 4-Nitropyridine N-oxide (POM), *J. Mol. Struct*. 738(1-3) (2005) 33–38. https://doi.org/10.1016/j.molstruc.2004.10.067.

[127] A.U. Hassan, S.H. Sumrra, M.F. Nazar, C. Güleryüz, A DFT Study on New Photovoltaic Dyes to Investigate their NLO Tuning at Near Infrared Region (NIR) as Pull–push Effect by End Capped Acceptors, *J Fluoresc*. 33 (2023) 239–253. https://doi.org/10.1007/s10895-022-03075-1.

[128] K.S. Kumar, N. Haridharan, S. Ranjith, A. Nataraj, Studies on the DFT calculations and molecular docking of versatile molecular sensor 1-(6-Aminopyridin-2-yl) -3-(4-nitrophenyl) urea, *Chemical Physics Impact*. 6 (2023) 100139. https://doi.org/10.1016/j.chphi.2022.100139.

Graphical abstract

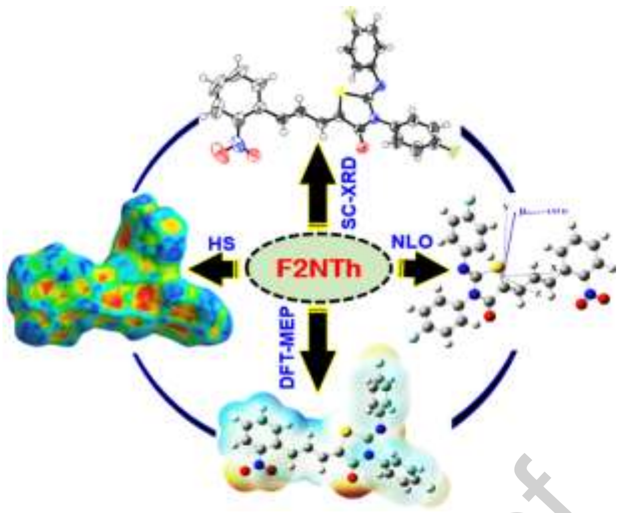

Author Contributions Section

N. Kheddam: Methodology, Investigation, Writing - review & editing.

A. Djafri: Synthesis, Writing - review & editing, Data curation.

Y. Megrouss: Methodology, Investigation, Software, Writing - review & editing, Formal analysis.

R. Rahmani: Investigation, Software, figures preparation.

A. R. Guerroudj: X-ray Data Processing, Structure Determination, CIF validation.

S. Belhachemi: Methodology, Investigation, Writing - review & editing.

A. Djafri: Synthesis, Supervision, Spectroscopic analysis, reviewing.

A. Chouaih: Supervision, Conceptualization, Methodology, review & editing.

Declaration of interests

X The authors declare that they have no known competing financial interests or personal relationships that could have appeared to influence the work reported in this paper.

☐The authors declare the following financial interests/personal relationships which may be considered as potential competing interests: